J. Fluid Mech. (2011), *vol.* 669, *pp.* 90–119. © Cambridge University Press 2011
doi:10.1017/S0022112010004945

Predicting the aftermath of vortex breakup in rotating flow

G. F. CARNEVALE[1]†, R. C. KLOOSTERZIEL[2], P. ORLANDI[3] AND D. D. J. A. VAN SOMMEREN[4]‡

[1]Scripps Institution of Oceanography, University of California, San Diego, La Jolla, CA 92093, USA

[2]School of Ocean and Earth Science and Technology, University of Hawaii, Honolulu, HI 96822, USA

[3]Dipartimento di Meccanica e Aeronautica, University of Rome, 'La Sapienza', via Eudossiana 18, 00184 Roma, Italy

[4]Eindhoven University of Technology, PO Box 513, 5600 MB Eindhoven, the Netherlands

(Received 20 May 2010; revised 17 September 2010; accepted 17 September 2010; first published online 11 January 2011)

A method for predicting the outcome of vortex breakup in a rotating flow is introduced. The vortices dealt with here are subject to both centrifugal and barotropic instabilities. The prediction of the aftermath of the breakup relies on knowing how both centrifugal and barotropic instabilities would equilibrate separately. A theoretical model for non-linear equilibration in centrifugal instability is wedded to two-dimensional simulation of barotropic instability to predict the final vortices that emerge from the debris of the original vortex. This prediction method is tested against three-dimensional Navier–Stokes simulations. For vortices in which a rapid centrifugal instability triggers a slower barotropic instability, the method is successful both qualitatively and quantitatively. The skill of the prediction method decreases as the time scales of the two instabilities become comparable.

Key words: geophysical and geological flows, turbulent flows, vortex flows

1. Introduction

Vortex breakup is a complicated process that often involves multiple instabilities. Nevertheless, in a rotating flow, the result of breakup and re-equilibration is usually a combination of simple vortex structures. Vortex monopoles, dipoles and tripoles, with their axes aligned along the ambient rotation axis, emerge out of the debris of the original vortex. Here, we consider the possibility of predicting the aftermath of vortex breakup based on our knowledge of the tendencies of the different instabilities involved.

Van Heijst & Kloosterziel (1989) and Kloosterziel & van Heijst (1991) investigated vortex breakup and re-equilibration in rotating tank experiments. The tank was filled with water with uniform density and then placed in rotation about a vertical axis. The fluid was allowed to reach a state of solid-body rotation. Then, an open-ended thin-walled hollow cylinder was placed vertically in the fluid. A vortex was created

† Email address for correspondence: gcarnevale@ucsd.edu

‡ Present address: BP Institute and Department of Applied Mathematics and Theoretical Physics, University of Cambridge, Cambridge CB3 0EZ, UK.

https://doi.org/10.1017/S0022112010004945 Published online by Cambridge University Press

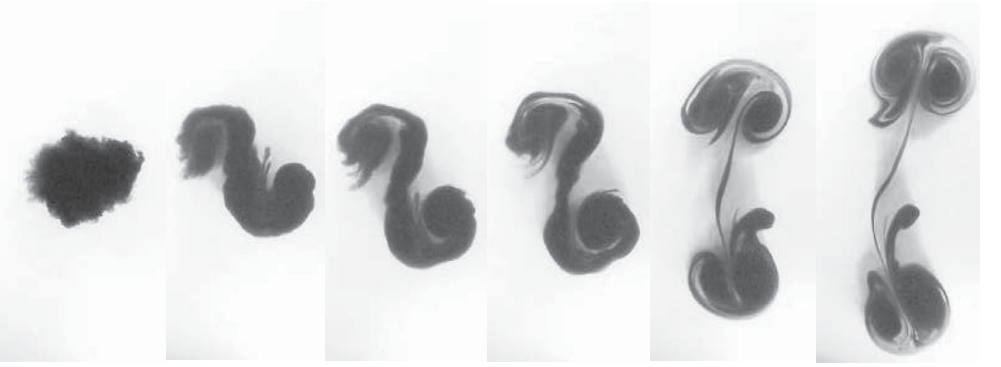


FIGURE 1. Breakup of an anticyclone leading to double dipoles in a laboratory experiment. The evolution takes place in 30 cm of water in a rotating tank. The photographs are taken from above with a camera in the rotating frame mounted on the axis of rotation. The leftmost photograph was taken shortly after the release of the dipole.

within the cylinder by stirring. An axially symmetric vortex was thus produced with azimuthal cyclonic or anticyclonic flow depending on the direction of the stirring. Dye was introduced in the confining cylinder to permit subsequent visualization of the flow. The vortex was then released by lifting the hollow cylinder vertically. Cyclones and anticyclones behaved rather differently from each other in these experiments. Just after release, the cyclones exhibited some three-dimensional motion on the periphery of the vortex, but the main flow remained predominantly two-dimensional (i.e. lacking vertical motion). The cyclones smoothly transitioned from the axisymmetric state into a tripole consisting of a central cyclone and two anticyclonic satellites. The anticyclones, in contrast, after release exhibited violent three-dimensional motions that persisted, and the horizontal structure became asymmetric. The flow then tended towards two-dimensionality while the vortex was torn apart horizontally, resulting in two vortex dipoles propagating away from each other, as shown in figure 1. The view in this figure is from above the flow, looking along the axis of rotation of the tank. The sequence of images from left to right shows the creation and evolution of the double-dipole state. The first image on the left of this figure shows the vortex shortly after release from the confining cylinder, and the last image shows two dipoles propagating away from each other.

Kloosterziel & van Heijst (1991) hypothesized that the evolution in these experiments could be understood as a combination of the effects of barotropic and centrifugal instabilities. The cyclones were initially centrifugally stable, or nearly so, and once released remained mainly two-dimensional, undergoing a barotropic instability leading to a tripolar state. The anticyclones were initially centrifugally unstable and the subsequent overturning motions led to strong horizontal vorticity gradients that triggered a stronger barotropic instability, which tore the anticyclone apart, leading to the formation of double dipoles.

Through three-dimensional numerical simulations, Orlandi & Carnevale (1999) reproduced the observed phenomenon and verified that, in fact, centrifugal instability in anticyclones does sharpen vorticity gradients, triggering the barotropic instabilities observed in the anticyclonic laboratory experiments. They also predicted that, for a certain range of Rossby number, the centrifugal instability of an anticyclone would not steepen the velocity profile sufficiently to result in double dipoles, but rather a tripole would form. Although rare in the type of experiment described above, this

https://doi.org/10.1017/S0022112010004945 Published online by Cambridge University Press

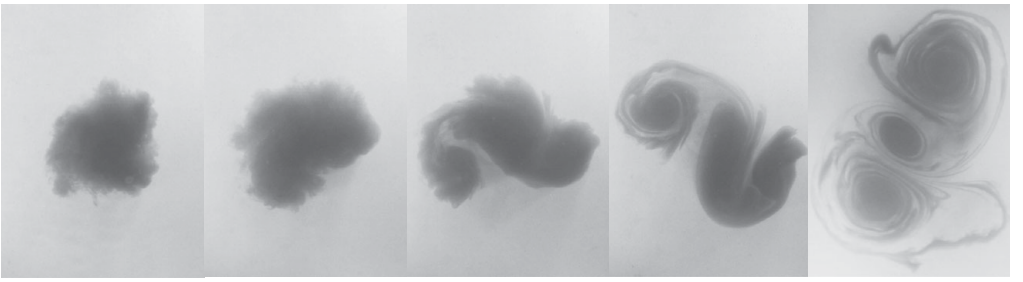


FIGURE 2. Breakup of an anticyclone leading to a tripole in a laboratory experiment. The evolution takes place in 30 cm of water in a rotating tank. The photographs are taken from above with a camera in the rotating frame mounted on the axis of rotation.

prediction was later verified in the laboratory. An example of tripole formation from an anticyclone is shown in figure 2.

Early in the development of this subject, there was a good theoretical understanding of barotropic instability and the end states that resulted due to nonlinear effects (cf. Dritschel 1986; Flierl 1988; Carton & McWilliams 1989; Carton, Fierl & Polvani 1989; Kloosterziel & Carnevale 1992; Carnevale & Kloosterziel 1994). Until recently, however, a comparable understanding of the nonlinear saturation of the centrifugal instability in unconfined vortices was lacking, even though there had been several detailed studies (e.g. Carnevale *et al.* 1997; Smyth & McWilliams 1998). Thus, no theoretical prediction could be made of the final result of the combined effect of the two instabilities. The missing piece of the puzzle has now been provided by Kloosterziel, Carnevale & Orlandi (2007*a*), who deduce a rule for the infinite-Reynolds-number equilibration of centrifugal instability. We will show how this rule can be combined with what is known of barotropic instability to make predictions about the combined effects of centrifugal and barotropic instabilities without resorting to costly three-dimensional simulations.

This work is motivated in part by the many oceanic examples of anticyclones that are marginally stable to centrifugal instability. These strong anticyclones are thought to be generated by frictional torques on strong currents passing coasts and islands (D'Asaro 1988). Some specific examples of these anticyclones are found in the wake of the island of Hawaii (Flament *et al.* 2001), in the wake of the Canary islands (Aristegui *et al.* 1994), and in the Beaufort Sea, where they have been created by flow through Barrow Canyon (D'Asaro 1988). All these vortices were probably centrifugally unstable when they were formed and then went through an adjustment that brought them to marginal stability. The work presented here is a contribution towards understanding that adjustment process. Our results could be the basis for parametrizing the effects of centrifugal instability in general circulation models with resolution too coarse to permit centrifugal instability.

The method of prediction developed here may be generalizable to systems other than vortices. A straightforward extension of this work would be to the prediction of the outcome of inertial instability in parallel shear flows. In the atmosphere, such instability is believed to cause phenomena like clear air turbulence (Knox 1997), rain bands or squall lines (Bennetts & Hoskins 1979), the banded structure of Jupiter's atmosphere (Stone 1967) and the vertically stacked temperature extrema near the equatorial stratopause (Hayashi, Shiotani & Gille 1998). In the equatorial pacific ocean, it may cause the observed 'interleaving' of alternately saltier and fresher layers

https://doi.org/10.1017/S0022112010004945 Published online by Cambridge University Press

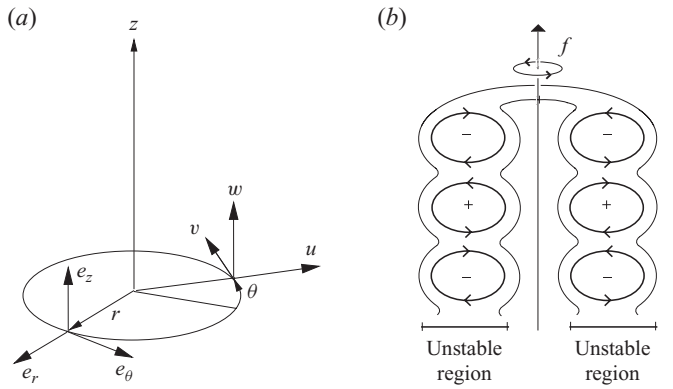


FIGURE 3. (*a*) Schematic diagram showing the cylindrical coordinate system. (*b*) A schematic representation of 'rib' vortices. The signs refer to the sign of the azimuthal vorticity ω_θ. The linear instability creates a stack of rings of azimuthal vorticity of alternating sign (rib vortices) centred on the axis of the primary vortex ($r = 0$). Note that $f = 2\Omega$ is the Coriolis parameter and Ω is the angular rotation rate of the ambient flow into which the vortex is introduced.

(Richards & Edwards 2003). We have already taken the first step towards developing a method for predicting the outcome of inertial instability on parallel shear flow in Kloosterziel, Orlandi & Carnevale (2007*b*), and further development analogous to that for vortices presented here will be the subject of future work.

The plan of this paper is as follows. In § 2, we briefly review the new theory of nonlinear equilibration of centrifugal instability and then outline relevant aspects of what is known about the nonlinear equilibration of barotropic instability. Then, in § 3 a scheme for combining the two theories of equilibration to make predictions of the outcome of the combined instabilities is given. In § 4, we test this theory in the most favourable situation, in which the centrifugal instability is much faster than the barotropic instability. To test the limits of this kind of prediction, in § 5 a less favourable case is explored for which the time scales of the two instabilities are similar. Conclusions are presented in § 6.

2. The basic instabilities

Both centrifugal and barotropic instabilities in their ideal form are not fully three-dimensional. Centrifugal instability is ideally an axisymmetric instability, while barotropic instability can be treated as a pure two-dimensional flow problem. In this section we will discuss basic characteristics of these two instabilities, focusing on how nonlinearities saturate these instabilities and lead to characteristic final stable states. We will begin with centrifugal instability and place special emphasis on the recent advances that allow the prediction of the equilibrated state in the high-Reynolds-number limit. The discussion of the barotropic instability will be a review of earlier work with emphasis on points relevant to this paper.

2.1. *Nonlinear equilibration in axisymmetric centrifugal instability*

In the breakup of anticyclones described in the Introduction, there is a vigorous three-dimensional instability during the early evolution. This three-dimensional phase is the result of centrifugal instability. To describe the evolution of the vortex, it is convenient to use a cylindrical coordinate system (r, θ, z) where the z-axis corresponds to the vertical direction (see figure 3*a*). The velocities (u, v, w) correspond to the radial,

https://doi.org/10.1017/S0022112010004945 Published online by Cambridge University Press

azimuthal and vertical directions. The components of vorticity in this coordinate system are given by

$$\omega_r = r^{-1}\partial_\theta w - \partial_z v, \quad \omega_\theta = \partial_z u - \partial_r w, \quad \omega_z = r^{-1}(\partial_r(rv) - \partial_\theta u). \tag{2.1}$$

An axisymmetric barotropic vortex with its axis coincident with the vertical axis is defined by the azimuthal velocity field $V(r)$. In the initially null field of azimuthal vorticity ω_θ, centrifugal instability creates a stack of vortex rings similar to the well-known toroidal Taylor–Couette vortices in the flow between concentric rotating cylinders. This perturbation appears and grows in an annular region of instability (see figure 3*b*) that can be defined through the Rayleigh criterion for centrifugal instability (Rayleigh 1916; Drazin & Reid 1981). The original version of this criterion was derived for axisymmetric flow in an inertial frame of reference. Subsequently, the criterion was generalized for vortices in a rotating frame (see Sawyer 1947; Kloosterziel & van Heijst 1991). Inviscid linear stability is determined by the distribution of the absolute angular momentum defined by $L \equiv r(V + \Omega r)$, where V is the azimuthal velocity of the flow, Ω is the ambient angular rotation rate and r is the radial distance from the axis of the vortex. The flow is unstable in an annulus where the magnitude of the absolute angular momentum decreases, in other words where $\mathrm{d}L^2/\mathrm{d}r < 0$.

We will base our discussion here on a family of vortices parametrized by a 'steepness parameter' α which controls the strength of the vorticity gradients outside the vortex core. The advantages of using this family are the following: namely all the vortices have zero circulation (hence finite energy); it can be used to match velocity profiles found in laboratory experiments reasonably well; its parameter α controls, to a great extent, the character of the instability; and it has been the subject of many previous theoretical and numerical investigations (e.g. Carton & McWilliams 1989; Carton *et al.* 1989; Orlandi & van Heijst 1992; Carton & Legras 1994; Carnevale & Kloosterziel 1994; Kloosterziel & Carnevale 1999; Orlandi & Carnevale 1999; Gallaire & Chomaz 2003). The velocity profile for this family is given by

$$V(r) = \pm\frac{r}{2}\exp(-r^\alpha), \tag{2.2}$$

where we have non-dimensionalized the velocity by a characteristic velocity $\mathscr{U}$ and radius by a length scale $\mathscr{L}$. The $\pm$ sign determines whether the vortex is a cyclone or anticyclone. The factor of $1/2$ normalization of the velocity is chosen to fix the non-dimensional vorticity at $r = 0$ to be $+1$ for cyclones and -1 for anticyclones. The vorticity derived from this velocity profile is aligned along the vertical direction. Its amplitude is given by

$$\omega_z(r) = \pm\left(1 - \frac{\alpha}{2}r^\alpha\right)\exp(-r^\alpha). \tag{2.3}$$

From the velocity and length scales $\mathscr{U}$ and $\mathscr{L}$, we define the Rossby and Reynolds numbers for this flow as

$$Ro = \pm\mathscr{U}/f\mathscr{L} \quad \text{and} \quad Re = \mathscr{U}\mathscr{L}/\nu, \tag{2.4}$$

respectively, where $f = 2\Omega$ is the Coriolis parameter. The Rossby number is defined so that the positive/negative sign corresponds to cyclones/anticyclones. In what follows, we have non-dimensionalized all spatial quantities using the length scale $\mathscr{L}$ and time with the advective time scale $\mathscr{L}/\mathscr{U}$.

For the anticyclonic case, figure 4 shows how the velocity V and vorticity ω_z profiles change with α. Note how vorticity gradients increase with increasing α. The graphs in the cyclonic case would be the same as these save for a sign change for the amplitude.

https://doi.org/10.1017/S0022112010004945 Published online by Cambridge University Press

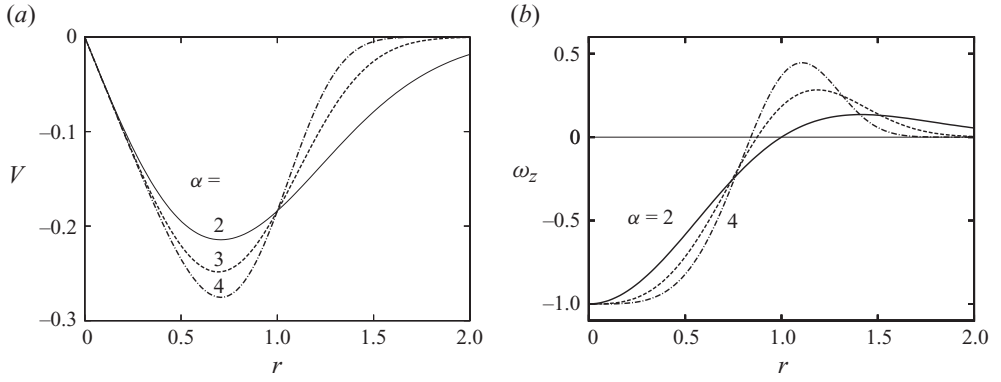


FIGURE 4. (*a*) Non-dimensional velocity profile from (2.2) for anticyclones. (*b*) Vertical vorticity profile corresponding to the velocity profile in (*a*). Lines: solid, $\alpha = 2$; dashed, $\alpha = 3$; dot-dashed, $\alpha = 4$.

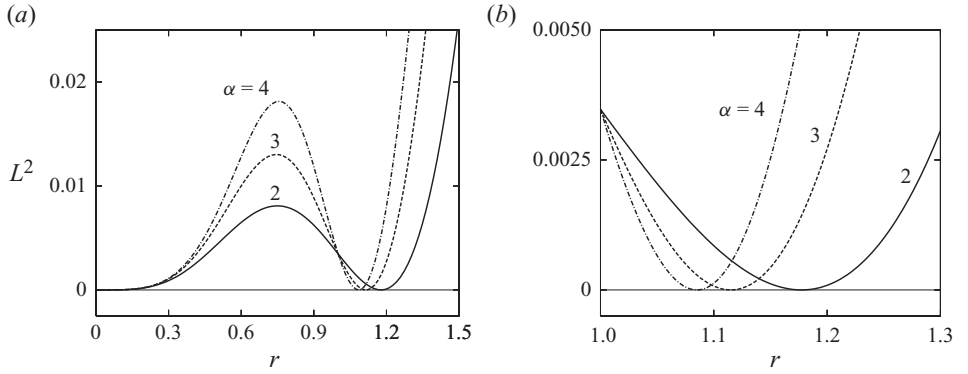


FIGURE 5. (*a*) The absolute angular momentum squared (L^2) for anticyclones with $Ro = -4$ for three values of α. The centrifugal instability region corresponds to the range of r where $\mathrm{d}L^2/\mathrm{d}r < 0$. (*b*) Zoomed image from (*a*) showing how the outer edge of the instability region varies with α for fixed Ro. Lines: solid, $\alpha = 2$; dashed, $\alpha = 3$; dot-dashed, $\alpha = 3$.

According to the Rayleigh criterion for centrifugal instability, a vortex with the profile (2.2) will be unstable to the formation of rib vortices if $Ro < -1$ or $Ro > Ro_{\mathrm{cr}}$, where

$$Ro_{\mathrm{cr}} = \frac{1}{\alpha} \exp\left(\frac{\alpha + 2}{\alpha}\right) \tag{2.5}$$

(Orlandi & Carnevale 1999).

For values of α and Ro for which this vortex is unstable, there is an annulus ($r^- < r < r^+$) in which the magnitude of angular momentum is decreasing. In figure 5(*a*), the behaviour of L^2 is shown for the case of the anticyclones shown in figure 4. Figure 5(*b*) shows how the outer edge of the instability region (that is, the point where $L = 0$) given by $r^+ = (\ln|Ro|)^{1/\alpha}$ moves inwards as α increases. We do not have a closed analytic formula for the position of the inner edge of the instability region r^-, which occurs at the local maximum of L^2. It is not a monotonic function of α, but from figure 5(*a*) we see that it is relatively insensitive to changes in α for the values of α presented. Using numerical methods, we find that the difference $r^+ - r^-$

https://doi.org/10.1017/S0022112010004945 Published online by Cambridge University Press

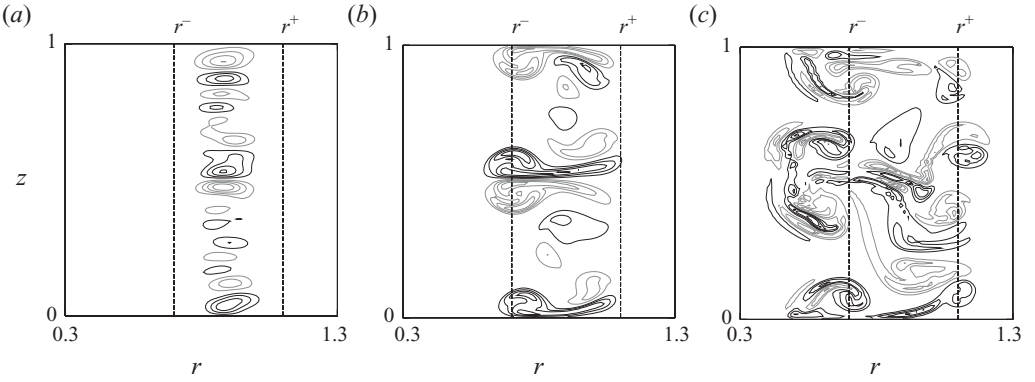


FIGURE 6. Overturning motions induced by centrifugal instability visualized by plots of azimuthal vorticity in an axisymmetric flow simulation. (*a*) ($t = 28$) The linear phase of the instability from random small-scale perturbations creates a stack of rings of azimuthal vorticity of alternating sign (rib vortices) centred on the axis ($r = 0$) of the primary vortex. (*b*) ($t = 56$) Nonlinear interactions of the rib vortices cause the formation of dipolar structures that propagate outside the initial unstable region. (*c*) ($t = 64$) Extensive mixing of angular momentum that extends well beyond the initial instability region results from the propagation of the perturbations. These are results for velocity profile (2.2) with $Ro = -4$ and $\alpha = 3$. The flow is bounded above (at $z = 1$) and below (at $z = 0$) by free-slip surfaces. The computational flow domain extends from $r = 0$ to $r = 6$. The boundary at $r = 6$ is also free-slip. The Reynolds number for this run was 6×10^4. Positive/negative contours of ω_θ are black/grey. The contour interval is 0.003. The range of the initial unstable region, $r^- < r < r^+$, is indicated by the vertical dashed lines.

is a monotonically decreasing function of α for $\alpha > 2$. In other words, for fixed Ro, the instability region becomes narrower as α increases.

Starting from small-scale random initial perturbations, the instability begins within the annulus of instability. The perturbation grows into a stack of 'rib vortices' as illustrated in the schematic diagram in figure 3(*b*), where we plot the azimuthal vorticity in an r–z (radial–vertical) cross-section. In inviscid theory, the most unstable rib vortices would be those of infinitesimal vertical dimension (Stone 1966; Dunkerton 1981; Bayly 1988; Smyth & McWilliams 1998; Gallaire & Chomaz 2003). However, the damping effect of viscosity on small scales results in a balance that selects a fastest-growing mode of finite scale that emerges from the linear phase of the instability. For increasing Re, the preferred vertical scale of the motions was found by Kloosterziel *et al.* (2007*a*) to decrease as $Re^{-1/3}$.

Kloosterziel *et al.* (2007*a*) studied the axisymmetric unfolding of centrifugal instability well beyond the initial linear phase. Their goal was to understand the ultimate tendency of the centrifugal instability acting alone. By using axisymmetric simulations, for which the barotropic instability is suppressed, they were able to follow the evolution of the pure (that is, axisymmetric) centrifugal instability all the way through to nonlinear equilibration. The numerical method will be discussed in § 4. The typical early phases of this axisymmetric evolution are illustrated in figure 6 taken from a numerical simulation at high Re. Figure 6(*a*) shows the rib vortices in the ω_θ field that grow out of the small-scale random perturbations during the linear dynamics phase of the instability growth. Note that these rib vortices are initially confined to the region of instability defined by the Rayleigh criterion. The limits of this region, $r^- < r < r^+$, are indicated by the dashed vertical lines in each figure. As the axisymmetric evolution continues past the linear-instability phase, the rib vortices

https://doi.org/10.1017/S0022112010004945 Published online by Cambridge University Press

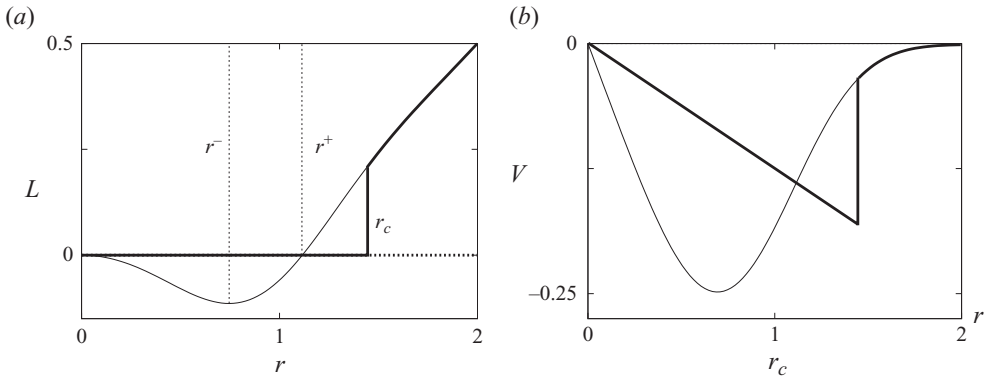


FIGURE 7. (*a*) A schematic diagram of the construction used to determine the new absolute angular momentum resulting from inviscid mixing of the angular momentum for a centrifugally unstable anticyclone in an example for which $\alpha = 3$ and $Ro = -4$. The thin curve is the absolute angular momentum of the original anticyclonic vortex. The thick curve is the equilibrated absolute angular momentum. The thick curve overlies the thin curve for $r > r_c$. (*b*) The azimuthal velocity field based on the equilibrated angular momentum shown in (*a*). The thin line is the initial velocity profile.

begin to pair, forming dipolar vortex heads in both the inner and outer parts of the instability region as seen in figure 6(*b*). The rib vortices then begin to self-advect beyond the linear-instability region, both towards smaller and larger r. As illustrated in figure 6(*c*), the dipolar heads propagate beyond the initial instability region. The rings then interact in a complicated fashion and soon engulf much of the vortex with overturning motions of the type observed in the laboratory experiment. Eventually this motion settles down, the flow becomes vertically uniform, the instability ceases, and there is a new distribution of angular momentum.

By running many axisymmetric simulations with many types of initial velocity profiles and a wide range of Reynolds numbers Re, Kloosterziel *et al.* (2007*a*) were able to deduce a rule for the final angular momentum distribution in the infinite Re limit. This rule says that for both cyclones and anticyclones the flow adjusts to reduce the gradient of L^2 in and around the region of initial instability. The adjustment involves mixing angular momentum from beyond the instability region into the instability region to produce constant L. It is surprisingly easy to predict just how far beyond the region of instability angular momentum will be mixed. For the anticyclone, the instability engulfs a region just large enough to bring the absolute angular momentum to zero everywhere in the new vortex core. This is illustrated in the diagram shown in figure 7(*a*). Equilibration is complete when the negative absolute angular momentum L is completely mixed with the positive L from the axis of the vortex out to a point $r = r_c$ that is just as far as necessary to make the total absolute angular momentum within that radius zero. Thus, given an initial anticyclonic profile $V_0(r)$, the value of r_c can be determined from the following formula:

$$\int_0^{r_c} L_0(r) r \, \mathrm{d}r = 0, \tag{2.6}$$

where $L_0(r) = r\,(V_0(r) + r/(2Ro))$ is the initial unperturbed absolute angular momentum.

The final equilibrated profile is then $L(r) = 0$ for $0 < r < r_c$, while $L(r) = L_0(r)$ for $r_c < r$. This profile is shown by the thick curve in figure 7(*a*). The corresponding

https://doi.org/10.1017/S0022112010004945 Published online by Cambridge University Press

prediction for the equilibrated velocity field is

$$V(r) = \begin{cases} -\dfrac{r}{2Ro}, & 0 \leqslant r \leqslant r_c, \\ V_0(r), & r_c < r. \end{cases} \tag{2.7}$$

Within the new core (i.e. where $r \leqslant r_c$), the predicted flow is given in dimensional form as $V(r) = -\Omega r$, which is just solid-body rotation with the angular velocity $-\Omega$, that is, the negative of the angular velocity of the tank. This means that the predicted flow in the core is stationary in the laboratory frame of reference. The profile for the equilibrated V is shown by the thick solid line in figure 7(b). This singular velocity profile is approached ever more closely in numerical axisymmetric experiments as the Reynolds number is increased (Kloosterziel *et al.* 2007*a*, figure 13*a*).

Cyclones can also be centrifugally unstable as noted above. However, centrifugal instability in barotropically stable cyclones cannot trigger barotropic instability. The difference between cyclones and anticyclones is discussed further in § 6.

2.2. *Nonlinear equilibration in 2-D Barotropic Instability*

The initial axisymmetric flow in an anticyclone has anticyclonic vorticity in the core surrounded by an annulus of cyclonic vorticity. In the later stages of the instability, this distribution is rearranged, in some cases rather dramatically. In the examples shown in the Introduction, a tripole and a pair of dipoles emerged out of the debris of the vortex breakup. More exotic structures such as quadrupoles (an anticyclone surrounded by three cyclonic satellites) have also been observed as temporary structures which then break up, leaving monopoles, dipoles or tripoles as stable byproducts of the breakup; see Morel & Carton (1994) and Carnevale & Kloosterziel (1994) for a fuller description of these possibilities.

The horizontal segregation of the vertical vorticity resulting in these structures is the result of barotropic instability. This is an instability of horizontal shear that can be understood completely within the context of two-dimensional flow. Since the instability is two-dimensional, it makes no difference if the initial flow is cyclonic or anticyclonic except for an overall sign change in the vorticity distribution. The (necessary) criterion for this instability is given by the inflection point theorem of Rayleigh (1880). Originally for planar shear, a generalized form of the criterion also applies to initially axisymmetric flow (see Drazin & Reid 1981). There is no known general sufficient criterion for the instability. Linear theory can be applied to piecewise uniform axisymmetric vorticity profiles to predict analytically the growth rates for various azimuthal modes, that is, modes that vary as $e^{im\theta}$. This was done by Stern (1987) and Flierl (1988) by normal modes analysis and by Kloosterziel & Carnevale (1992) through an energy method. For more general profiles, as would be appropriate for laboratory flows, numerical analysis can be used to predict the growth rates of individual azimuthal modes. The barotropic instability of velocity profile (2.2) has been studied as a model for laboratory flows as well as for geophysical flows. For this profile, figure 8 shows how the growth rates of the first three unstable modes vary with the steepness parameter (cf. Carton & McWilliams 1989; Carnevale & Kloosterziel 1994; Gallaire & Chomaz 2003). These are measured exponential amplification rates of the perturbations that follow $\exp(\gamma t)$ with t the non-dimensionalized time. There are no growing modes for $\alpha \lesssim 1.85$. As α is increased above this critical value, mode $m = 2$ is the first to become unstable. The growth of this mode is responsible for tripole formation. As α is increased further, higher modes also become unstable. The double-dipole formation seen in the Introduction results from the growth of a

https://doi.org/10.1017/S0022112010004945 Published online by Cambridge University Press

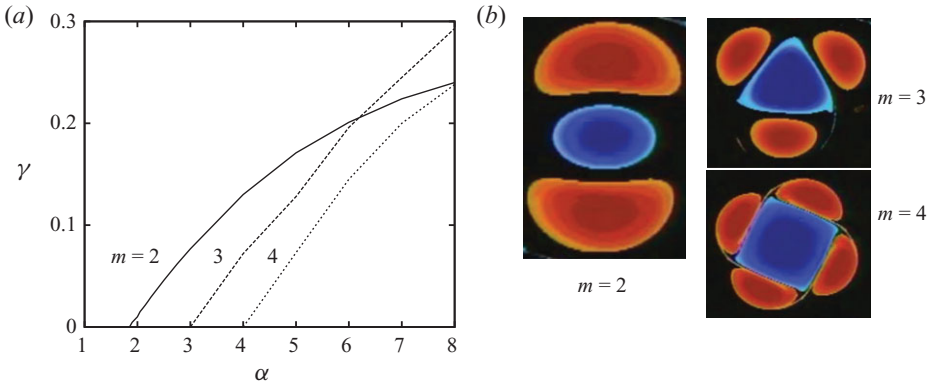


FIGURE 8. (*a*) Non-dimensional exponential growth rate γ of the barotropic instability for azimuthal modes $m = 2, 3, 4$ (data from Kloosterziel & Carnevale 1999). (*b*) Products of nonlinear evolution when the initial perturbation is purely mode $m = 2$ (tripole), 3 (quadrupole) or 4 (pentapole). Blue/red represents positive/negative vorticity.

combination of mode $m = 2$ and higher modes, and so can occur only for $\alpha \gtrsim 3$. Carnevale & Kloosterziel (1994) showed that mode $m = 3$ may grow into a stable quadrupole, but its stability was rather fragile, and small disturbances of a few per cent of its maximum vorticity led to its destruction. Because of its fragile stability, the quadrupole is not ordinarily seen as an end state of the kind of anticyclone breakup described above; however, Beckers & van Heijst (1998) have shown that it is possible to routinely generate quadrupoles in the laboratory by strongly stimulating mode $m = 3$ initially, in agreement with the numerical study by Carton (1992). The mode $m = 4$ growth can result in creating a pentapole (as in figure 8). This 'square vortex' becomes unstable when fluctuations bring two of the outer satellites close together. The satellites then coalesce in pairs, forming a transient tripole that then usually breaks up into a pair of dipoles. Higher-order structures, resulting from the growth of higher-order azimuthal modes, also become unstable when the outer satellites come close together and coalesce, resulting in some combination of monopoles, dipoles and tripoles.

The long-term outcome of the barotropic instability will depend on the value of α as well as the distribution of initial perturbation energy among the possible unstable modes for that value of α. For $\alpha \lesssim 1.85$, the flow is not unstable and remains a monopole. A tripole results for $1.85 \lesssim \alpha \lesssim 3$ (Kloosterziel & Carnevale 1999). For higher values, the vortex can go through a remarkable array of forms, depending on how many azimuthal modes are unstable and the precise form of the initial perturbation. Very complicated flows can result, especially when the initial perturbation has significant energy in spatial scales on the order of that characteristic of the unperturbed vortex. The flow can evolve through a series of intermediate states including, for example, hexapoles, pentapoles and quadrupoles. Except for small-scale debris in the form of thin vorticity filaments and the small vortices that may be created by the roll-up of filaments, the final result is some combination of monopoles, dipoles, tripoles and quadrupoles, although the quadrupole is a less likely component as discussed above. If the initial disturbance is made of only small-scale small-amplitude randomly distributed velocity fluctuations, we find that the end product is either a monopole, a tripole or a pair of dipoles.

https://doi.org/10.1017/S0022112010004945 Published online by Cambridge University Press

3. Full 3-D simulation versus prediction

Our goal is to determine how well the outcome of the breakup of an anticyclonic vortex can be predicted by using what we know of the nonlinear equilibration of the axisymmetric centrifugal instability and the 2-D barotropic instability. In the laboratory experiments discussed above, it appears that an early rapid centrifugal instability sets up conditions for a barotropic instability that then follows. For inviscid flow, we can predict the outcome of pure centrifugal instability by using (2.7). Here we will use this formula to give us an approximation of the effects of centrifugal instability in the early part of the actual 3-D flow. Then, lacking a general theory to predict the equilibration of barotropic instability, we use 2-D simulation of the Navier–Stokes equations to predict the outcome of the barotropic instability. The initial condition for this 2-D simulation is taken as the theoretical equilibrium of the centrifugal instability and random grid-scale noise. The 3-D viscous flow will never actually achieve the velocity discontinuity contained in (2.7). Therefore, perhaps one should consider using an artificially smoothed version of this profile for an initial condition of the 2-D simulation. The singular profile could be smoothed by estimating the diffusive effect of viscosity acting over some period of time or perhaps, more simply, the discontinuity could be arbitrarily smoothed over the scale of a few gridpoints. Either choice would be artificial and arbitrary, so for the time being we have used formula (2.7) as is, simply rendering it on the finite 2-D grid used in the next phase of the prediction. The Reynolds number used for the 2-D simulation is that of the 3-D simulation to which the prediction will be compared. The grid for the 2-D simulation is the same as the horizontal grid used in the 3-D simulation.

In summary, this prediction scheme replaces the centrifugal instability phase of the evolution by jumping to the velocity field given by (2.7). Then the barotropic instability phase of the flow is replaced by a two-dimensional simulation. This scheme has the best chance of succeeding when the initial flow is centrifugally unstable but barotropically stable. In that case, in the full 3-D simulation, the flow must become centrifugally unstable before any barotropic instability can take place. Thus, we take as our first case an initial profile with steepness parameter $\alpha = 1.8$, which is barotropically stable as discussed in § 2.2 above. On the other hand, the prediction scheme should be expected to have less skill if the initial instability rates for the two instabilities are comparable. How well the scheme does under these circumstances will be tested using an example with $\alpha = 3$. In both cases, we have explored a range of Re and Ro as will be discussed below.

4. Centrifugal instability faster than barotropic instability ($\alpha = 1.8$)

As explained above, the velocity profile (2.2) is barotropically stable for $\alpha \lesssim 1.85$. If we take as an initial condition the velocity profile (2.2) with $\alpha = 1.8$, there will be no barotropic instability initially. There will, however, be centrifugal instability if the Rossby number is sufficiently negative. The inviscid criterion tells us that we will have centrifugal instability if and only if $Ro < -1$; however, since we cannot reproduce infinite Re flow numerically, we must consider the effects of finite Re.

The numerical method used is a finite-difference staggered-mesh scheme that solves the incompressible Navier–Stokes equations in a cylindrical coordinate system (r, θ, z) with the z-axis coincident with the axis of the initial vortex, which is parallel to the axis of rotation of the background as sketched in figure 3. The details of the method, which is energy conserving in the absence of viscosity in the limit of infinitesimal time steps, are described in detail in Verzicco & Orlandi (1996) and Orlandi (2000). We impose

https://doi.org/10.1017/S0022112010004945 Published online by Cambridge University Press

free-slip boundary conditions on the top and bottom of the computational domain and on the cylindrical wall. To allow sufficient room for the unfolding of the barotropic instability, we have taken the radial range as $0 < r < 6$. The coordinate system is stretched in the radial direction to allow for a uniform maximal radial resolution up to $r = 2$ and gradually diminishing resolution for larger r. Changing the stretching to begin beyond $r = 2.25$ showed no significant effect on the results when applied in test cases. In the vertical direction, sufficient space is needed to represent the rib vortices discussed above. This is more of a concern at low Re than at high Re because the rib vortices are thinner in the vertical direction the higher the value of Re. For high Re, the concern is to have sufficient resolution in the vertical direction to resolve the rib vortices. Our previous experience with axisymmetric simulations (Kloosterziel *et al.* 2007*a*) and 3-D simulations (Orlandi & Carnevale 1999) of centrifugal instability suggested that the vertical range $0 < z < 1$ would be adequate for present purposes. Each 3-D simulation was initiated with the ideal velocity profile (2.2) and a random perturbation of amplitude 1 % of $V(r)$ was applied to the azimuthal velocity at every point in the domain. Perturbations of much lower amplitude were found to be too weak to initiate instability before the vertical vorticity diffused significantly, especially at low values of Re. Thus, this 1 % perturbation level was used in all simulations.

Simulations were performed from $Re = 5000$ (i.e. 5k) to $Re = 30$k. Problems with insufficient resolution become marked at $Re = 20$k and were unacceptable at $Re = 30$k. The adequacy of the resolution was tested both by examining how quickly energy falls off in spectral space during the most turbulent phase of the breakup (see the Appendix for more details) and by grid refinement. The grid-refinement tests involved comparing the end results of key simulations using grids with N grid points in each of the three coordinate directions with N varied from 97 to 129 to 193. It was found that the simulations with $N = 129$ were well resolved up to and including $Re = 15$k. The results reported throughout the paper are based on simulations with $N = 129$.

Through 3-D simulation, we find that for $\alpha = 1.8$ at $Re = 15$k, the centrifugal instability is insufficient to induce barotropic instability from $Ro = -1$ down to $Ro \approx -2.05$, while tripoles form for $-2.05 \gtrsim Ro \gtrsim -2.45$ and double dipoles for $-2.45 \gtrsim Ro$. We will now examine two examples in some detail.

4.1. *Example: tripole formation:* $\alpha = 1.8$, $Ro = -2.35$

We begin with a case of evolution that leads to a tripole. Before looking at the final outcome of the instability, it is interesting to examine the effects of the initial instability, which in this case must be centrifugal. A centrifugally unstable vortex evolving three-dimensionally will suffer a much more complicated initial development than that possible in axisymmetric flow due to the potential for unstable modes with non-zero azimuthal wavenumber. The evolution of the azimuthal component of the vorticity is a useful diagnostic, at least for the early flow, because initially there is no ω_θ associated with the basic profile (2.2). The growth of the rib vortices discussed in the Introduction is well captured by growth in ω_θ. To help analyse the complex evolution, we decompose the azimuthal vorticity perturbation field $\omega_\theta(r, \theta, z, t)$ into azimuthal 'm' and vertical 'k-modes' according to

$$\hat{\omega}_\theta(r, m, k, t) = \int_{\theta=0}^{2\pi} \int_{z=0}^{1} \omega_\theta(r, \theta, z, t) \sin(2\pi k z) \mathrm{e}^{-\mathrm{i}m\theta} \, \mathrm{d}z \, \mathrm{d}\theta. \tag{4.1}$$

https://doi.org/10.1017/S0022112010004945 Published online by Cambridge University Press

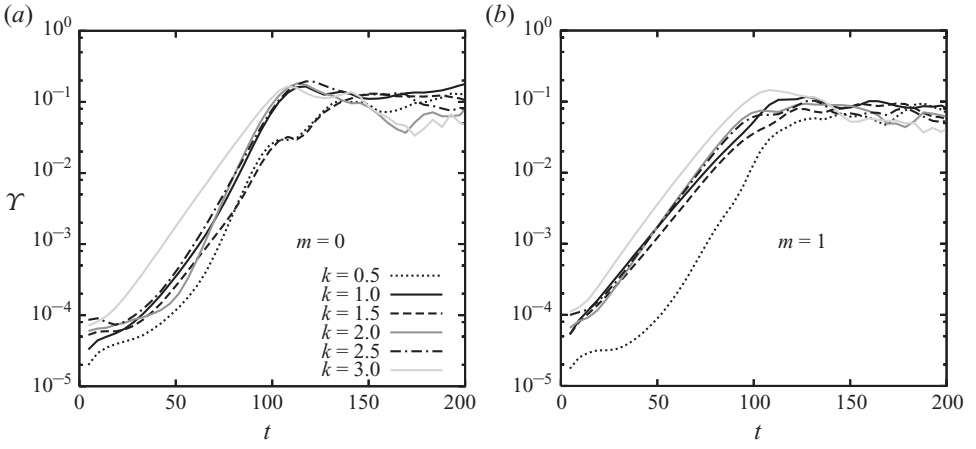


FIGURE 9. History of $\Upsilon_{k,m}$ as defined by (4.2) for vertical wavenumbers $k = 0.5, 1, \ldots, 3.0$, with azimuthal mode wavenumbers (*a*) $m = 0$ and (*b*) $m = 1$ for the case $\alpha = 1.8$ and $Ro = -2.35$.

The integrals are performed as discrete sums over our computational grid. The axial wavenumbers k are positive half-integers ($k = 1/2, 2/2, 3/2, \ldots$). Note that it is convenient to use the sine transform in the vertical direction because the free-slip boundaries force $\omega_\theta = 0$ at $z = 0$ and $z = 1$. The azimuthal wavenumbers are signed integers ($m = 0, \pm 1, \pm 2 \ldots$), but note that because ω_θ is real, the Hermiticity condition $\hat{\omega}^*(r, m, k, t) = \hat{\omega}(r, -m, k, t)$ holds.

A measure of the contribution of a certain mode (k, m) in the azimuthal vorticity can be defined as

$$\Upsilon_{k,m}(t) = \sqrt{\frac{\displaystyle\int_{r=0}^{r=r_{rib}} |\hat{\omega}_\theta(r, k, m, t)|^2 r \, \mathrm{d}r}{r_{rib}^2/2}}, \tag{4.2}$$

where r_{rib} is to be taken sufficiently large to fully capture the effects of the instability on the vortex. The actual value of r_{rib} will depend on the parameter values for a particular simulation. We found that taking $r_{rib} = 1.5 r_c$, where r_c is defined by (2.6), is sufficient. The normalization is such that if $|\hat{\omega}_\theta(r, k, m, t)| = 1$ over the region of integration, then $\Upsilon_{k,m}$ would be unity. The growth rate $\sigma_{k,m}(t)$ of a certain mode (k, m) in this region can be defined by

$$\sigma_{k,m}(t) = \frac{\mathrm{d}}{\mathrm{d}t} \ln(\Upsilon_{k,m}(t)). \tag{4.3}$$

The time-varying contribution $\Upsilon_{k,m}$ and the growth rate $\sigma_{k,m}$, apart from the normalization, are as defined by Gallaire & Chomaz (2003), who performed a linear-stability study for vortices over a range of α but without background rotation. They found that of all modes, those with $m = 0$ and $m = 1$ are the fastest growing with the growth rate of the mode $m = 0$ being about 10 % larger than that of the corresponding $m = 1$ mode. With rotation, we also find that modes $m = 0, 1$ dominate. In figure 9, we show the evolution of $\Upsilon_{k,m}$ for $m = 0, 1$ for $k = 0.5$ to $k = 3$. Unlike the case of the linear analysis of Gallaire & Chomaz (2003), where each mode exhibits exponential growth, here the modes display a more complicated behaviour, although each shows some period of exponential growth somewhere between $t = 0$ and $t \approx 90$. During this period, mode $(m, k) = (0, 2)$ achieves the highest growth rate ($\sigma_{2,0} = 0.15$ at $t = 68$).

https://doi.org/10.1017/S0022112010004945 Published online by Cambridge University Press

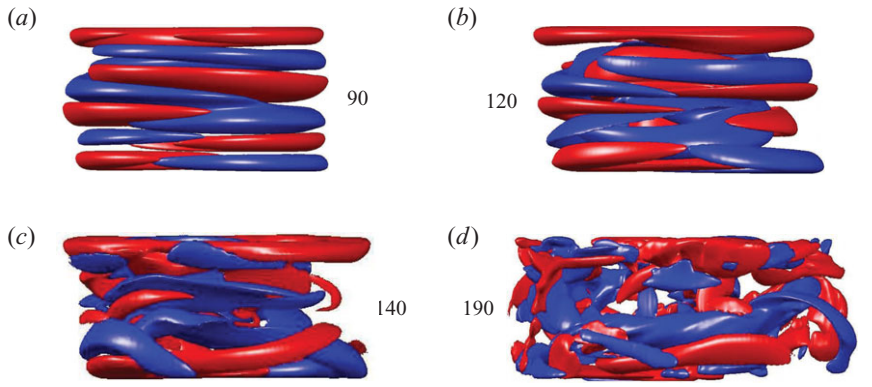


FIGURE 10. (*a–d*) Three-dimensional isosurfaces of the azimuthal vorticity ω_θ distribution for the case with $\alpha = 1.8$, $Ro = -2.35$ and $Re = 15$k. The images are views taken from a direction perpendicular to the axis of the primary vortex and correspond to different times as labelled. The structure of the rib vortices is well organized until $t \approx 120$, and azimuthal modes $m = 0$ and $m = 1$ are identifiable. After $t \approx 140$, the rib vortices tangle and a description in terms of a few azimuthal modes is no longer possible. Red/blue corresponds to positive/negative ω_θ with magnitude increasing in time from 3.2×10^{-3} at $t = 90$ to 3.3×10^{-1} at $t = 190$.

The highest growth rate attained by an $m = 1$ mode is about 25 % lower ($\sigma_{0.5,1} = 0.11$ at $t = 92$). Of the modes shown, the $m = 0$ modes tend to grow at least 20 % more rapidly than the $m = 1$ modes for the corresponding values of k, except for the $k = 6$ modes, where the maximum growth rates are about the same for $m = 0$ and $m = 1$. The highest amplitude is achieved by an $m = 0$ mode ($\Upsilon_{2.5,0} \approx 0.2$ at $t = 120$). After $t \approx 90$, nonlinear effects end the exponential growth phase of these modes. Until this time, the perturbation can be described essentially in terms of the $m = 0$ and $m = 1$ modes; however, after this time, higher azimuthal modes reach similarly high amplitudes and become important in a way that is best illustrated with three-dimensional vorticity isosurface plots.

Figure 10 shows the early evolution of the instability for $\alpha = 1.8$ and $Ro = -2.35$ through a rendering of the azimuthal component of the vorticity. The image at $t = 90$ shows the field that results from the exponential growth phase of the instability. The next image shows that modes with azimuthal wavenumbers $m = 0$ and $m = 1$ continue to dominate until about time $t = 120$. After this point, the rib vortices become entangled and much higher azimuthal modes become significant. The entanglement of the rib vortices is a result of strong nonlinear interactions.

Although the early instability is not the ideal centrifugal instability, which is purely axisymmetric with only $m = 0$ modes, the essential result is, nevertheless, still a steepening of vorticity gradients similar to that seen in axisymmetric simulations. In figure 11, we show the initial velocity and angular momentum profiles (dashed) and compare them with the vertically and azimuthally averaged profiles at later times. The dotted curve in each figure represents the theoretical equilibrium for axisymmetric flow in the $Re = \infty$ limit. The vertical lines at radii r^- and r^+ indicate the inner and outer boundaries of the initial centrifugally unstable region. The figure shows the tendency of the 3-D instabilities to steepen the velocity and angular momentum profiles, in the region beyond $r = r^+$, and to bring the core into solid-body rotation. For this simulation, the time $t = 140$ represents the point of maximum steepening of these curves in the outer region. Subsequent evolution showed relaxation towards solid-body rotation for $r < r^+$ and diminishing of the velocity gradient beyond r^+.

https://doi.org/10.1017/S0022112010004945 Published online by Cambridge University Press

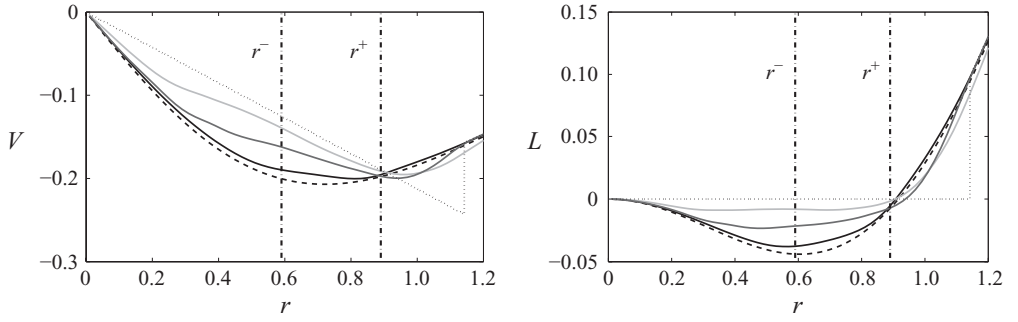


FIGURE 11. The radial profile of the vertically averaged azimuthal velocity and angular momentum of the vortex from the 3-D simulation with $\alpha = 1.8$, $Ro = -2.35$ and $Re = 15$k. The curves correspond to times $t = 0$, 90, 140 and 190. The initial $t = 0$ profile is shown by a black dashed line (– – – –) and the later times by solid lines with shading from black to light grey of decreasing intensity with increasing time. The theoretical profile of the vortex after stabilization by the axisymmetric centrifugal instability at infinite Reynolds number is shown by a dotted line (·····). The inner and outer radii (r^-, r^+) of the initial centrifugally unstable region are denoted by the dash-dotted (—·—) vertical lines.

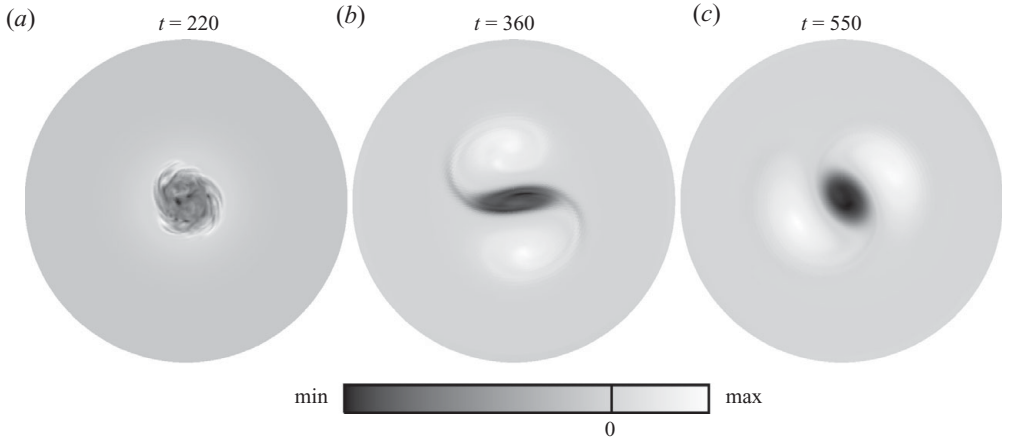


FIGURE 12. (*a–c*) Evolution of ω_z averaged over z for the case $\alpha = 1.8$, $Ro = -2.35$ and $Re = 15$k. The corresponding figure showing the evolution of azimuthal power is 13(*a*). The limits on the grey-scale vary between minimum and maximum values that change with time: $t = 220$ (min $= -2$, max $= 1$), $t = 360$ $(-1.2, 0.6)$ and $t = 550$ $(-1.2, 0.4)$. The full horizontal extent of the computational domain out to $r = 6$ is shown.

Of course, at any finite Re, the steepening of the gradients can never reach the predicted infinite slope. The change of the averaged velocity profile with Re is discussed in detail by Kloosterziel *et al.* (2007*a*). Although the steepening of the gradient is incomplete, it is sufficient, as we will see, to trigger barotropic instability in accord with the hypothesis of Kloosterziel & van Heijst (1991) and in agreement with Orlandi & Carnevale (1999).

As the centrifugal instability steepens the velocity gradient, various barotropically unstable modes begin to grow. The effect on the vortex can be seen in the vertically averaged vertical component of the vorticity field $\bar{\omega}_z(r, \theta, t)$ shown in figure 12. By $t = 220$, a large-scale distortion away from axisymmetry is just becoming noticeable. By $t = 360$, a tripole has formed, but at this point it is difficult to know whether this

https://doi.org/10.1017/S0022112010004945 Published online by Cambridge University Press

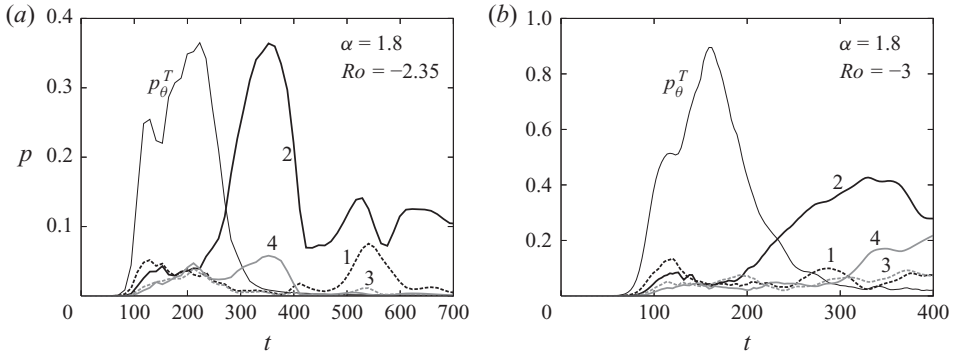


FIGURE 13. Evolution of the power $p_{z,m}$ in azimuthal modes of ω_z. The thick labelled curves show the evolution of power in azimuthal modes 1–4 (dashed black line, $m=1$; solid black line, $m=2$; dashed grey line, $m=3$; solid grey line, $m=4$). The thin solid line is the total power in ω_θ. All curves are normalized by the instantaneous power of the axisymmetric component (i.e. $|\omega_{z,0}(t)|^2$). For (*a, b*) $\alpha=1.8$ and $Re=15$k. (*a*) The case $Ro=-2.35$ is an example for which a tripole results. (*b*) The case $Ro=-3$ is one for which a pair of dipoles results.

vortex will remain a tripole or split into a pair of dipoles. However, the subsequent evolution is simply continued rotation and viscous diffusion of the tripole.

To analyse this behaviour in detail, we can compare the 'power', that is variance, in the various azimuthal modes of $\bar{\omega}_z(r,\theta,t)$ with that in the axisymmetric ($m=0$) mode. We define the modal amplitude as

$$\tilde{\omega}_{z,m}(t) \equiv \int_{\theta=0}^{2\pi}\int_{r=0}^{r_{max}}\int_{z=0}^{1} \omega_z(r,\theta,z,t)\mathrm{e}^{-\mathrm{i}m\theta} r\,\mathrm{d}r\,\mathrm{d}\theta\,\mathrm{d}z, \tag{4.4}$$

where the integration is over the entire computational domain. For the simulations reported here, $r_{max}=6$. The Fourier transform in θ is performed using a fast Fourier transform and the integrals in r and z are computed as sums on the discrete computational grid. The ratio of the contribution of modes m and $-m$ relative to the axisymmetric part of the flow is

$$p_{z,m}(t) \equiv \frac{|\tilde{\omega}_{z,m}|^2 + |\tilde{\omega}_{z,-m}|^2}{|\tilde{\omega}_{z,0}|^2} = 2\frac{|\tilde{\omega}_{z,m}|^2}{|\tilde{\omega}_{z,0}|^2}, \tag{4.5}$$

where we have used the Hermiticity constraint to simplify. In addition, it is useful to consider the total power in the ω_θ-field relative to that in the axisymmetric part of ω_z. This will give us a measure of the importance of centrifugal instability, which generates ω_θ. Thus, we define the total power in ω_θ relative to that in the axisymmetric part of ω_z:

$$p_\theta^T(t) \equiv \frac{1}{|\tilde{\omega}_{z,0}|^2}\int_{\theta=0}^{2\pi}\int_{r=0}^{r_{max}}\int_{z=0}^{1} \omega_\theta^2(r,\theta,z,t) r\,\mathrm{d}r\,\mathrm{d}\theta\,\mathrm{d}z. \tag{4.6}$$

In figure 13(*a*), the evolution of the power in the most highly excited azimuthal modes of the vertically averaged vertical vorticity ω_z is plotted along with p_θ^T. We first note that rapid growth in p_θ^T precedes growth in the azimuthal modes of ω_z. Departure of the vortex from axisymmetry is measured by the power $p_{z,m}(t)$ in modes $m\neq 0$. After $t=100$, there is some significant growth in modes $|m|=1, 2, 3$ and 4 that all remain at about the same level until around $t=220$; however, they each have less than 5 % of the power compared with the axisymmetric mode. The combined effect of these azimuthal modes does not yet cause a very strong distortion of the vortex away from

https://doi.org/10.1017/S0022112010004945 Published online by Cambridge University Press

axisymmetry, as we see remains the case in figure 12 at $t = 220$. Then, around $t = 220$, $p_{z,2}(t)$ begins to grow rapidly. When this reaches about 10 %, a tripole is seen to begin to emerge, and by $t = 360$, we have the well-formed tripole shown in figure 12 at that time. Note that $p_{z,4}(t)$ grows to about the 5 % level around $t = 360$. This is related to a thinning of the central anticyclonic vortex. As $p_{z,4}(t)$ subsequently decreases, the central vortex becomes more circular. Even though $p_{z,2}(t)$ decreases to about the 10 % level after it has peaked at $t = 360$, it remains the dominant mode, and the vorticity configuration remains that of a tripole as shown in figure 12 at $t = 550$. At time $t = 550$, $p_{z,1}(t)$ is near its peak value and seems to rival $p_{z,2}(t)$; however, this seems to have little effect on the form of the tripole. As an aside, we note that modes $m = \pm 1$ are interesting in that they are never unstable in the pure barotropic problem (see figure 8). Their growth is made possible only with the freedom of variation in z and they play an important role in the 3-D centrifugal instability, as discussed above. In the barotropic problem, they can be related to the propagation of the vortex structure since they correspond to a dipolar perturbation, and a dipolar distribution of ω_z would exhibit self-induced motion. In the centrifugal instability, on the other hand, these modes change the axisymmetric ring modes of the pure centrifugal instability into helical modes.

4.2. *Double-dipole formation:* $\alpha = 1.8$, $Ro = -3$

For sufficiently negative Rossby numbers ($Ro \lesssim -2.45$ with $Re = 15\text{k}$), the evolution of the vortex becomes more complicated and more interesting. Figure 13(b) shows the histories of the power in the first four perturbation azimuthal modes of ω_z along with the total power in ω_θ for a simulation with $Ro = -3$. With $\alpha = 1.8$, there is still no initial barotropic instability, and as in the previous case, we see that rapid growth in $p_\theta^T(t)$ precedes growth in the azimuthal modes of ω_z. Also as in the previous case, eventually there is significant growth and sustained amplitude in $p_{z,2}(t)$. The most significant difference between figures 13(a) and 13(b) is that in figure 13(b) we see an appreciable sustained growth in $p_{z,4}(t)$. To see how this affects the evolution of the vortex, we will now compare the evolution of the ω_z vorticity distribution shown in figure 14 with the modal power histories in figure 13.

In figure 14, we see that around $t = 210$ the distribution of ω_z has formed a triangular core of anticyclonic vorticity surrounded by three cyclonic satellites, a quadrupole. This is related to the growth of $p_{z,3}(t)$, which peaks at about 8 % and is around 6 % at $t = 210$ (see figure 13b). Such a triangular structure has been the subject of previous theoretical study, numerical simulations and laboratory experiments (Carnevale & Kloosterziel 1994; Beckers & van Heijst 1998). This configuration with three cyclonic satellites can persist indefinitely if the initial perturbation is carefully prepared and dominated by mode $m = 3$; however, for random initial conditions as used here, this is usually just a transient phase of the evolution. As discussed by Morel & Carton (1994) and Carnevale & Kloosterziel (1994), the quadrupole becomes unstable when two of its satellites come close to each other and merge, as is about to happen at $t = 210$. The subsequent merger seen in figure 14 around $t = 225$ results in a configuration in which $p_{z,2}(t)$ dominates, that is a tripole. Unlike the previous case, with $Ro = -2.35$, where the central vortex eventually becomes more circular, here the central vortex, being strongly sheared by the outer satellites, becomes more elongated. It eventually rolls up into two anticyclones that pair with the two cyclonic satellites, as seen in figure 14(e, f). The resulting pair of dipoles has a significant mode $m = 4$ component along with mode $m = 2$. The growth of $p_{z,4}(t)$ in figure 13(b) corresponds to this formation of the

https://doi.org/10.1017/S0022112010004945 Published online by Cambridge University Press

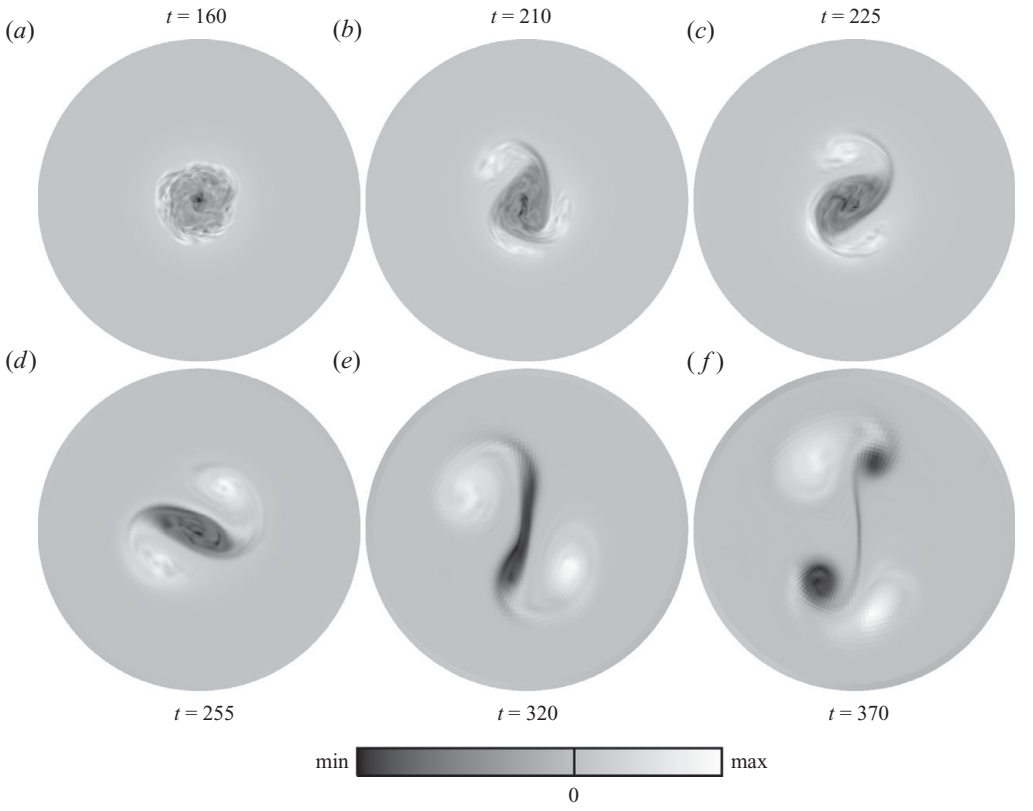


FIGURE 14. (*a–f*) Evolution of ω_z averaged over z for the case $\alpha = 1.8$, $Ro = -3$ and $Re = 15$k. The corresponding figure showing the evolution of azimuthal power is 13(*b*). The limits on the grey-scale vary between minimum and maximum values that change with time: $t = 160$ $(-4, 2)$, $t = 210$ $(-2.5, 1.5)$, $t = 225$ $(-2, 1)$, $t = 255$ $(-1.5, 1.0)$, $t = 320$ $(-1.2, 0.8)$ and $t = 370$ $(-1.2, 0.8)$.

double-dipole structure. After about $t = 400$, the propagating dipoles begin to interact with the walls of the domain. For simulations with more negative Ro at the same α, the behaviour is similar to that shown in figure 14, except that the early formation of a quadrupole may be preceded by the formation of structures of higher order, that is, structures with even more satellites. As with the quadrupole, these too become unstable with the merger of the outer satellites. Eventually, the merger process results in the formation of double dipoles, as shown in the late stages in figure 14.

4.3. *Testing the prediction:* $\alpha = 1.8$

Next, we test whether the combined effect of centrifugal and barotropic instabilities can be predicted based solely on our inviscid prescription for centrifugal instability and two-dimensional simulations of barotropic instability, as explained in § 3. In figure 15(*a*), we show the contour plot of the vertical vorticity at mid-depth for a fully 3-D simulation of the evolution. The flow at this stage is nearly uniform in the vertical direction. We show the mid-depth field here rather than a vertically averaged field to allow some of the small-scale features to be evident. Furthermore, we have used contour plots rather than grey-scale to allow a somewhat more detailed comparison between the 3-D simulation and the prediction.

https://doi.org/10.1017/S0022112010004945 Published online by Cambridge University Press

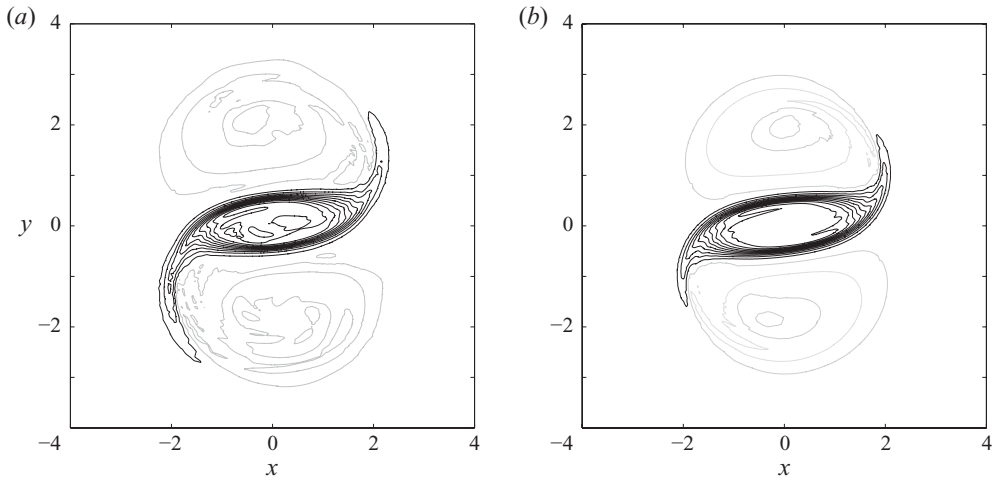


FIGURE 15. Comparison of the results of the three-dimensional simulation with the prediction. (*a*) Vorticity field at mid-depth at time $t = 380$ in the fully three-dimensional simulation. (*b*) Predicted vorticity field at time $\tau = 330$ from the two-dimensional simulation of the barotropic part of the prediction. The isolevels increase from -0.5 to 0.3 with increments of 0.04. Black/grey contours represent negative/positive isolevels. $\alpha = 1.8$, $Ro = -2.35$ and $Re = 15$k.

At this point in the evolution of the flow, the centrifugal instability has run its course, and the barotropic instability has been triggered and finally equilibrated, resulting in a tripole. For comparison, the vorticity distribution from our prediction is given in figure 15(*b*). The time scales are different in the two cases. Figure 15(*a*) corresponds to the 3-D simulation at time $t = 380$ after the initial condition, while the time $\tau = 330$ in figure 15(*b*) is the time since the initiation of the 2-D simulation starting from the theoretical centrifugal equilibrium state. The 3-D result and the prediction are remarkably similar. Note that the overall orientation of the fields is not significant since it only depends on the particular orientation of the field of random perturbations used to initiate the flow.

Next, we consider the $Ro = -3$ case, which, as seen above, results in double dipoles. Since this is still a case with $\alpha = 1.8$, the initial profile is again barotropically stable and it is the centrifugal instability that drives the flow towards barotropic instability. The result of a full 3-D simulation is illustrated by the vertical vorticity at mid-depth in figure 16(*a*). This can be compared with the prediction in figure 16(*b*), based again on our inviscid prescription for centrifugal instability equilibration followed by the 2-D simulation. Even though the vorticity minima in the anticyclones are somewhat more diffuse in the prediction than in the 3-D simulation, overall the results match very well.

4.4. *Regime diagram:* $\alpha = 1.8$

Another measure of the skill of our prediction scheme is how well it can predict the boundaries between the regimes in which the final result of evolution from small-scale random initial perturbations is a monopole, a tripole or double dipoles. The results depend on the Reynolds number. Our predictions are based on the inviscid extrapolation for centrifugal instability and should thus improve as Re increases. On the other hand, for a given resolution, the numerical simulations will degrade in quality as Re is increased and small scales are not properly represented, thus limiting the accessible range of Re.

https://doi.org/10.1017/S0022112010004945 Published online by Cambridge University Press

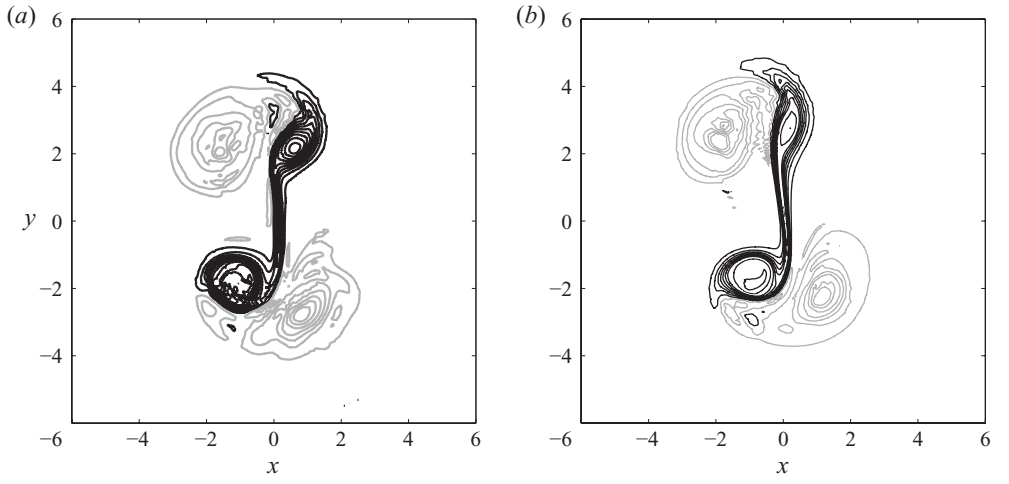


FIGURE 16. Comparison of the results of the three-dimensional simulation with the prediction. (*a*) Vorticity field at the mid-depth at time $t = 360$ in the fully three-dimensional simulation. (*b*) Predicted vorticity field at time $\tau = 240$ from the two-dimensional simulation of the barotropic part of the prediction. The isolevels increase from -0.4 to 0.2 with increments of 0.03. Black/grey contours represent negative/positive isolevels. $\alpha = 1.8$, $Ro = -3.0$ and $Re = 15$k.

We have performed a series of 3-D simulations designed to map out the boundary between the regimes in which small-scale random perturbations of our basic profile will lead to a final monopole, a tripole or double-dipole configuration. The 3-D simulations were compared with our prediction scheme described above using 2-D simulation. The resolution of both the 3-D and 2-D simulations was 129 points in each coordinate direction.

Determining the border between the tripole regime and the double-dipole regime was very straightforward. For simulations near this border, the flow reaches a point at which a tripole forms with an elongated elliptical anticyclone in the centre and two cyclonic satellites. The flow is then at a critical point in the evolution. One of two very different scenarios follows. In one scenario, the anticyclone continues to elongate and then rolls up into two anticyclones. Each of these 'daughter' anticyclones then partners with one of the cyclonic satellites to create one of the dipoles in the resulting double-dipole configuration. In the other scenario, the elongation of the central anticyclone ceases and is followed by 'axisymmetrization' (Melander, McWilliams & Zabusky 1987) of the central vortex. In the latter scenario, the resulting configuration remains a tripole with a nearly circular central vortex during the long viscous decay phase that follows.

The double-dipole states are generally not as symmetric as that shown in figure 14 at $t = 370$. In some cases, one of the dipoles is composed of a very strong vortex and a very weak vortex. For a given Ro and Re that produce a double-dipole state, the degree of symmetry of the dipoles is sensitive to the choice of the seed for the random generation of the initial small-scale perturbation. When one of the vortices in a dipole is very weak, it may become sheared out around the stronger companion vortex, and the resulting final state of the system may look more like a dipole and a separate monopole than two dipoles. We have not tried to create a separate category for these states but just consider them as examples of the limiting case of asymmetry in the double-dipole state.

https://doi.org/10.1017/S0022112010004945 Published online by Cambridge University Press

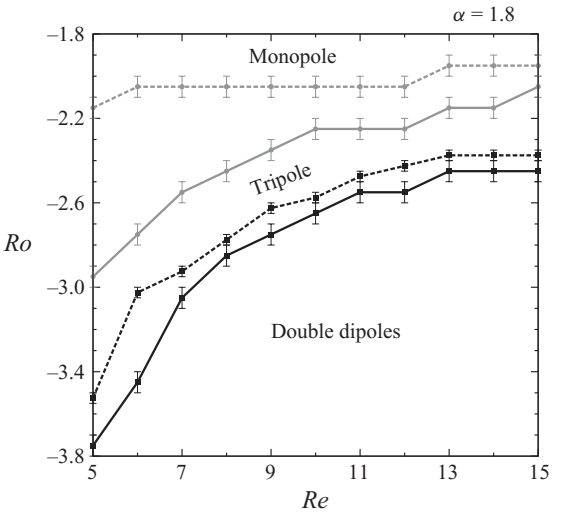


FIGURE 17. Regime diagram for the case with $\alpha = 1.8$, in which the centrifugal instability is initially faster than the barotropic instability. The solid black curve is the boundary between tripoles and double dipoles resulting from 3-D simulations. The dashed black curve is the prediction for this boundary. The solid grey curve is the boundary between monopoles and tripoles resulting from 3-D simulations. The dashed grey curve is the prediction for this boundary. The sampling error is indicated by the error bars. *Re* is given in units of 1000.

Determining the border between the monopole and the tripole regimes proved less straightforward than for the tripole to double-dipole transition. The problem here is that some mode $m = 2$ growth may be observed without the formation of well-defined cyclonic satellites. One needs to somewhat arbitrarily decide how much mode $m = 2$ distortion of the monopole is necessary to classify it as a tripole rather than a monopole. Barba & Leonard (2007) confronted this issue in a study of the emergence of tripoles from vortices with net circulation. In their definition of a tripole, they required that the zero-vorticity contour pinches off, isolating the two satellite vortices from each other. We considered using this criterion, but found that in our case of zero net circulation, the zero contour line was rather more complicated, and we found it difficult to precisely state whether it closed around each of the satellites or not. For example, sometimes it would close around one satellite but not around the other, or just nearly close, with the formation of many thin filaments that made the contour difficult to follow. A detailed discussion of this filamentation and its dynamic implications is found in Carton & Legras (1994). We considered using other contour levels. At levels below 0.05 (which is 5 % of the unperturbed $|\omega_z|$ at $r = 0$), we found that some ambiguity remained in some cases. At level 0.05, there was no ambiguity in deciding when the contours pinched off or not for any of the simulations near the transition boundary. The states in which this contour pinched off seemed reasonably described as tripoles. Testing with a contour level 0.06 and above, we found some states in which the contour did pinch off unambiguously, but for a vorticity distribution that looked very much like a monopole with only a weak mode-2 perturbation. Thus, 0.05 seemed a reasonable choice, and we decided to deem the structure a tripole when this contour pinched off.

The regime diagram resulting from the 3-D simulations is shown in figure 17 along with our predictions. The solid curves with solid symbols are deduced from the 3-D simulations. The regime boundary predictions are shown by dashed curves. The

https://doi.org/10.1017/S0022112010004945 Published online by Cambridge University Press

curves are drawn by plotting the average of Ro of the two simulations that define the transition from one behaviour to the other at a given Re. For example at $Re = 15\text{k}$, a tripole was found for $Ro = -2.5$ and double dipoles at $Ro = -2.6$. Thus, the regime boundary was marked at the midpoint $Ro = -2.55$. One could thus assign an error to this point as $\Delta Ro = \pm 0.05$, which is just the sampling error. The sampling error is indicated by the error bars on each data point.

The curves in figure 17 imply that the smaller Re the larger Ro needs to be to obtain a transition from the monopole state. This seems reasonable since a Laplacian viscosity will damp the azimuthal modes more than the axisymmetric mode (the higher m the more efficient the damping). There is a trade-off between high viscosity (damping) at low Re and the large amount of available energy that can be released at large Ro, making transitions possible at small Re if Ro is sufficiently large. For fixed $Ro \lesssim -2.6$, the graphs of the 3-D results show that as Re increases, one goes from monopoles to tripoles to double dipoles. This reflects the fact that as Re increases, the damping on mode $m = 2$, the mode necessary to create a tripole, becomes insufficient to prevent its growth to significant levels, while mode $m = 4$ is still suppressed, and thus a tripole results. Then for even higher Re, mode $m = 4$ is able to grow and double dipoles result. Although mode $m = 3$ is also barotropically unstable, and its growth would also be expected, it typically leads to a transient configuration as explained in § 2.2. Similarly, modes with $m > 4$ also become important as Re is increased, but they too lead to structures that are unstable and transient. The tendency of the curves in the high-Re limit is not entirely clear. We do not have data beyond $Re = 15\text{k}$ that is sufficiently well resolved to say whether the regime boundaries asymptote to two distinct values in the $Re \to \infty$ limit or if perhaps they both converge towards $Ro = -1$, in which case we would always find double dipoles after centrifugal instability at $Re = \infty$.

Figure 17 reveals that for fixed Re, the gap in Ro where tripoles result is relatively narrow compared with the ranges in which double dipoles or monopoles result, both of which extend beyond the limits of the figure. This may account for the fact that in early experimentation with anticyclones produced by stirring in a rotating tank (Kloosterziel & van Heijst 1991), only monopoles or double dipoles were observed as final states.

In terms of the validity of our predictions, we should expect that at low Re the difference between 3-D simulations and our prediction, which is based in part on inviscid projections for the centrifugal instability, is relatively large but improves with increasing Re. We see that this is the case, for example, for the monopole to tripole boundary. At low Re, viscous effects diminish the ability of the centrifugal instability to steepen the velocity profile. Thus, it is more difficult to produce the higher azimuthal modes needed to produce tripoles than in the inviscid case, and so tripole production requires a higher Ro than predicted. As Re increases, the effects of viscosity become less important and the gap between prediction and 3-D simulations diminishes, plateauing for $Re \geqslant 10\text{k}$, before shrinking to the size of the sampling error at $Re = 15\text{k}$. A similar trend is found for the tripole to double-dipole transition boundary. For that boundary, the gap between prediction and 3-D simulations becomes about the sampling error for $Re \geqslant 8\text{k}$. For both boundaries, the prediction systematically underestimates the magnitude of Ro needed to achieve transition for a given Re because finite Re does not permit the full steepening of the vorticity gradients that the prediction assumes. Nevertheless, the success is remarkable, and we would expect that the gap between prediction and 3-D simulations would decrease further with increasing Re, given sufficient numerical resolution.

https://doi.org/10.1017/S0022112010004945 Published online by Cambridge University Press

5. Barotropic instability faster than centrifugal instability ($\alpha = 3$)

For α higher than 1.85, the growth rate of the barotropic instability will be non-zero from the initial moment. In that case, centrifugal instability and barotropic instability will be in competition from the beginning. One can imagine that as long as the centrifugal instability is substantially faster than the barotropic instability, our prediction scheme should continue to exhibit skill in predicting the outcome of the combined instability. However, the prediction scheme should lose skill as the growth rate of the initial barotropic instability increases to and exceeds that of the centrifugal instability. Here we test how well the scheme does in the situation when the growth rate of barotropic instability is initially somewhat larger than that of centrifugal instability.

The barotropic instability growth rate for mode $m = 2$ (the mode responsible for tripole production) acting alone is approximately 0.077, as shown in figure 8(a). Note that since the Coriolis parameter does not enter into the 2-D flow equations, the growth rate for the barotropic instability has no dependence on the Rossby number. The growth rate of the centrifugal instability, however, does depend on the Rossby number of the flow. The growth rate for the pure centrifugal instability may be obtained by performing axisymmetric simulations. For $\alpha = 3$ and $Re = 15$k, we find that as Ro is decreased from $Ro = -1.0$ to $Ro = -2.2$, the growth rate of the centrifugal instability increases from 0.0 to 0.073. Thus, in this range of Ro, the centrifugal instability is slower than the barotropic instability.

As we shall see, the transition from the tripole regime to the double-dipole regime occurs at $Ro \approx -1.45$, which falls in this range of Ro. Furthermore, for $\alpha = 3$, the barotropic instability is sufficiently strong that tripoles form for all Ro from $Ro = -1$ (the inviscid centrifugal instability boundary) down to the tripole to double-dipole transition boundary. Thus, there is no monopole to tripole regime transition boundary in this case.

Examining the evolution of the azimuthal modes provides some insight into the dynamics, as in the $\alpha = 1.8$ case. First, we consider a case that results in a tripole. We take $Ro = -1.3$ as an example. In figure 18(a), we see the evolution of $p_{z,m}(t)$ (defined by (4.5)) for $m = 1$–4 as well as $p_\theta^T(t)$. Since in this case all of the power levels are very small except for $p_{z,2}(t)$, we plot the graphs on a logarithmic scale to facilitate comparison between them. The first thing to note is that the barotropic instability is evident early on with $p_{z,2}(t)$ growing much more rapidly than p_θ^T. The strong growth of mode $m = 2$ results in the formation of a tripole. Note that p_θ^T never becomes more than a tenth of a per cent (10^{-3}). The flow begins to take the form of a tripole as $p_{z,2}(t)$ reaches 10 % at around $t = 130$. It is a well-defined tripole at $t = 170$, when $p_{z,2}(t)$ is at its maximum, and remains a well-defined, although slowly decaying, tripole after that. Mode 4 grows rapidly until about $t = 150$; however, $p_{z,4}(t)$ remains small (less than 3 %) and so the structure is dominated by mode $m = 2$ and the flow remains a tripole.

Next, we look at the azimuthal modal growth in a case which results in double dipoles. We take $Ro = -1.46$ as an example. In contrast with the previous case, here we do see early growth in p_θ^T that competes with the growth in mode $m = 2$ and reaches over 10 % before decaying, suggesting that centrifugal instability plays a significant role. A tripole forms around $t = 145$, when $p_{z,2}(t)$ has reached 10 %. As $p_{z,4}(t)$ reaches 10 % at $t = 220$, the central anticyclonic vortex becomes elongated, and by $t = 233$, with $p_{z,4}(t)$ reaching 15 %, the elongated anticyclone rolls up, forming two anticyclones that go into creating the final pair of dipoles, similar to those shown in figures 14 and 16. Although at $\alpha = 3$, mode $m = 2$ can grow even in the absence of

https://doi.org/10.1017/S0022112010004945 Published online by Cambridge University Press

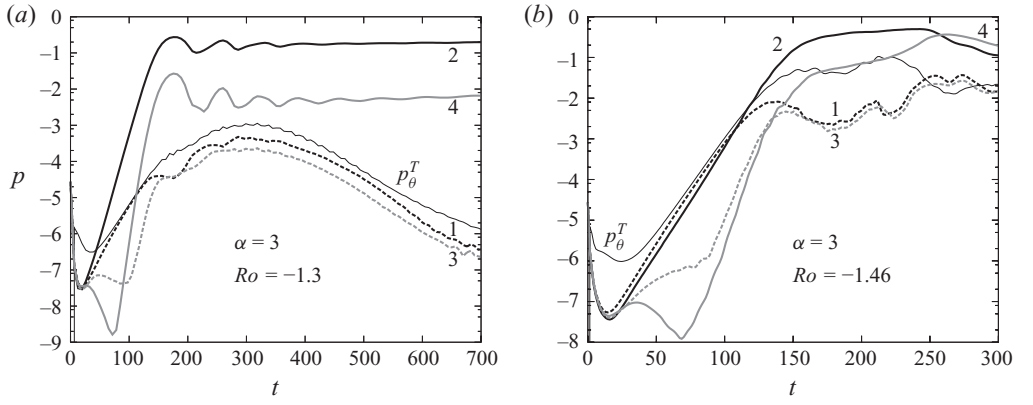


FIGURE 18. Evolution of the power $p_{z,m}$ in azimuthal modes of ω_z. The thick labelled curves show the evolution of power in azimuthal modes $m = 1$–4 (dashed black line, $m = 1$; solid black line, $m = 2$; dashed grey line, $m = 3$; solid grey line, $m = 4$). The thin solid line is the total power in ω_θ. All curves are normalized by the instantaneous power $|\omega_{z,0}(t)|^2$. For each panel, $\alpha = 3$ and $Re = 15$k. (*a*) The case $Ro = -1.3$ is an example in which a tripole is produced. (*b*) The case $Ro = -1.46$ is one for which double dipoles result. The p-axis is logarithmic.

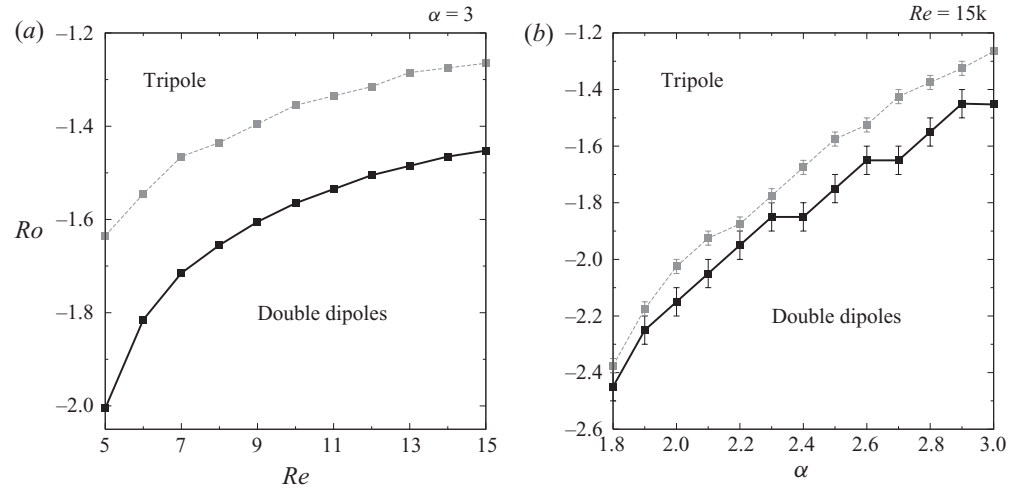


FIGURE 19. (*a*) The regime diagram for the case with $\alpha = 3$ in which the barotropic instability is initially faster than the centrifugal instability. The thick solid curve results from 3-D simulations. The thin dashed curve is the prediction. Error bars are not included because the sampling error is $\Delta Ro = \pm 0.005$ or less and the error bars would be obscured by the symbols on the lines. Re is given in units of 1000. (*b*) Variation of the regime boundary with α. The thick solid curve results from 3-D simulations. The thin dashed curve is the prediction.

centrifugal instability, while mode $m = 4$ cannot (see figure 8). Thus, it is the effect of the centrifugal instability that allows growth in mode $m = 4$, and this growth will only happen if the centrifugal instability (here measured by p_θ^T) is sufficiently strong.

5.1. *Regime diagram:* $\alpha = 3$

In figure 19(*a*), we compare the predicted boundary for the transition from the tripole regime to the double-dipole regime with that found with 3-D simulation. Although

https://doi.org/10.1017/S0022112010004945 Published online by Cambridge University Press

the curves have similar tendencies, the predicted curve systematically underestimates the magnitude of Ro. The sampling error on these curves is $\Delta Ro = \pm 0.005$, much less than in the case $\alpha = 1.8$ and much less than the separation of the curves. The 3-D $\alpha = 3$ simulations proved less costly in computer time than the $\alpha = 1.8$ simulation, because the velocities involved for runs near the regime boundaries are lower (because $|Ro|$ is lower in this case), and this allowed more simulations to be run for this case and, hence, higher precision in determining the regime boundary.

As for the case with $\alpha = 1.8$, the gap between prediction and 3-D simulation decreases with increasing Re, here going from $\Delta Ro = 0.370$ to 0.1875 as Re goes from 5k to 15k. In other words, the prediction improves with increasing Re. The gap at $Re = 15$k is, however, larger than that for the case of the $\alpha = 1.8$ tripole to double-dipole transition border which is 0.075. This is perhaps what we should expect given the competing roles here of centrifugal and barotropic instabilities from $t = 0$, as discussed above.

Overall, it is remarkable that even though in this case the barotropic instability is somewhat faster than the centrifugal instability, the prediction at least captures the form of the regime boundary. Attempts to match the shape of the curves in figure 19(a), as well as those in figure 17, to simple power laws in Re did not prove fruitful. Additional experiments reaching to $Re = 30$k show that the gap between prediction and simulation continues to narrow as Re increases; however, the issue of grid resolution with $Re > 15$k is as in the case of the $\alpha = 1.8$ simulations, and we feel that those simulations are not sufficiently resolved to be presented here. The systematic underestimation of Ro by the prediction in figure 19(a) is not surprising, for two reasons. First, as we have discussed for the case of $\alpha = 1.8$, the prediction is based on an infinite Re centrifugally equilibrated V that is discontinuous. Such a discontinuous profile will have higher growth rates for $m = 2$ and higher modes than the smoothed profiles that would actually result from a finite-Re simulation. Second, for $\alpha = 3$, the centrifugal instability will not have time to steepen vorticity gradients as much as it would if the barotropic instability were slower.

5.2. *Regime boundary as a function of* α

To quantify how the dependence of the difference between prediction and 3-D simulation grows with increasing α at fixed Re, we present, in figure 19(b), the tripole to double-dipole transition Ro as a function of α for both our prediction and our 3-D simulation results. The graph shows that for $Re = 15$k and increasing α, the gap between prediction and 3-D simulation opens up from $\Delta Ro = 0.075$ at $\alpha = 1.8$ to $\Delta Ro = 0.1875$ at $\alpha = 3$. This trend can be expected to continue since with increasing α the barotropic instability will become ever faster. The best results are for low α where the centrifugal instability is much more rapid than barotropic instability. However, this graph suggests that for sufficiently high Re, there is a wide range of α for which the prediction scheme is fairly skilful.

6. Conclusion

We have presented a new method for predicting the final vortices that emerge from the breakup of a centrifugally unstable vortex in a rotating flow. This method consists of first theoretically predicting the velocity profile towards which centrifugal instability acting alone in an axisymmetric inviscid flow would drive the vortex. This theoretical prediction uses a simple construction based on angular momentum conservation. The resulting velocity profile is then used as the initial state of a

https://doi.org/10.1017/S0022112010004945 Published online by Cambridge University Press

two-dimensional simulation that captures the subsequent barotropic instability. We have shown that this prediction method is very accurate when the initial vortex is such that the centrifugal instability is much faster than any initial barotropic instability. We have given a quantitative indication of how much skill this prediction method loses as the initial growth rate of barotropic instability relative to that of centrifugal instability is increased, and we have shown that, at least within one family of vortices, the method still works reasonably well even when these initial growth rates are not very different. This prediction method is a synthesis of what has been learned about centrifugal and barotropic instabilities in rotating flow over the last few decades. The field has progressed considerably since the first insights into the interaction between centrifugal and barotropic instabilities were presented in Kloosterziel & van Heijst (1991).

The success of the prediction method suggests that some version of it may prove a useful tool in situations in which computing resources are insufficient to fully resolve centrifugal instability. For example, in a general circulation model, a vortex may appear that would be centrifugally unstable at infinite resolution, but will not become unstable simply because the resolution of the model is insufficient to allow centrifugal instability. The theoretical prediction for the centrifugally equilibrated vortex could be substituted for such a vortex. This would then trigger the appropriate subsequent barotropic instability, if any. Thus, the effects of a process which could be modelled only at much higher resolution could be directly incorporated in the under-resolved model.

We have not discussed here the case in which barotropic instability is much faster than the centrifugal instability. One can imagine, for example, starting with a flow that is barotropically unstable but centrifugally stable. The subsequent evolution could increase the curvature of the flow which could trigger a centrifugal instability. Bayly (1988) proved that the centrifugal instability condition can be applied locally with the radius of curvature of streamlines playing the role of the radius in axisymmetric flow. When the barotropic instability produces flow curvature sufficient to create centrifugal instability, it is expected that the flow would locally go centrifugally unstable and attempt to redistribute angular momentum, perhaps in such a way as to increase local vorticity gradients. It would be interesting to try to predict the effect of such a secondary centrifugal instability in modifying the primary barotropic instability in such a scenario, but such a line of research has, as far as we are aware, never been pursued.

Centrifugal instability in cyclones results in a velocity profile less steep than it was originally, that is, stability is achieved by decreasing velocity gradients, just the opposite of what happens in the anticyclonic case. Since transforming a barotropically stable state into a barotropically unstable state requires steepening velocity gradients, centrifugal instability in the cyclonic case cannot trigger a barotropic instability. This point has been discussed in detail by Kloosterziel *et al.* (2007*a*). Furthermore, in the case of the cyclone, the redistribution of angular momentum during centrifugal instability does not reach deep into the core of the vortex, but instead is confined to a narrow neighbourhood of the unstable region that is at the outer edge of the core of the vortex. This, together with the fact that for cyclones Ro may need to be significantly greater than 1 for centrifugal instability (see (2.5)) while $|Ro| > 1$ suffices for anticyclones, explains why 'explosive' three-dimensional instability was observed in anticyclones but not cyclones in the rotating tank experiments by Kloosterziel & van Heijst (1991).

Although all of the work presented above was based on homogeneous (i.e. constant-density) flow, our predictions may also work for centrifugally unstable barotropic vortices in stratified flow with uniform background stable density gradient.

https://doi.org/10.1017/S0022112010004945 Published online by Cambridge University Press

Kloosterziel *et al.* (2007*a*) have shown that the results of axisymmetric centrifugal instability with or without background stratification are the same as long as the Reynolds number is sufficiently high. Stratification changes the form of the rib vortices (flatter rib vortices for higher stratification) and the time scale of centrifugal instability, but at high Reynolds numbers, the instability results in the same redistribution of angular momentum as found in the unstratified case. However, possible decoupling between layers in the vertical direction may lead to some difference in the evolution in the barotropic instability part of the evolution. How well the unstratified predictions work in the stratified case would be worth testing in future work. Considering baroclinic vortices (i.e. vortices with vertical shear) in stratified flow would introduce another level of complication. We are currently developing a prediction scheme for the outcome of centrifugal instability for baroclinic vortices. This is much more difficult than in the barotropic vortex case in stratified flow, where the unperturbed isopycnals are flat. In the baroclinic case, mixing of angular momentum takes place along isopycnals that are not horizontal and the mixing results in changing the shape of the isopycnals. Further progress must be made on this problem before predictions similar to those given above can be made.

Finally, we note that Kloosterziel *et al.* (2007*b*) give a prescription for predicting the effect of centrifugal instability on rotating planar shear flows. As mentioned in the Introduction, it may be possible to use this prediction in a scheme to predict the outcome of a fully 3-D flow starting with a planar shear flow. The prediction of Kloosterziel *et al.* (2007*b*) could be used to replace the centrifugal instability phase of the flow and then 2-D simulations based on the predicted profile may capture the subsequent evolution to some extent.

G.F.C. and R.C.K. acknowledge support from the National Science Foundation grants OCE 07-26482 and OCE 07-26866, respectively. D.D.J.A.v.S. acknowledges support from Dr Hendrik Muller's Vaderlandsch Fonds and TU/e FSB.

Appendix. Resolution test

In the test of the adequacy of the grid resolution at high Re, we take the Fourier sine transform of the vertical velocity w at a radius inside the instability region. We define an azimuthally averaged amplitude at $r = 1$ as

$$\bar{w}_k(t) = \frac{1}{2\pi} \int_{\theta=0}^{2\pi} \int_{z=0}^{1} w(r = 1, \theta, z, t) \sin(2\pi k z)\, \mathrm{d}z\, \mathrm{d}\theta. \tag{A 1}$$

The axial wavenumbers k are positive half-integers ($k = 1/2, 2/2, 3/2, \ldots$). The Fourier sine transform in z is performed using a fast Fourier transform on our discrete computational grid, and the integral in θ is calculated by discretization on the grid. The resulting power spectrum $\bar{w}_k^2$ is plotted in figure 20 for different values of Re and different computational resolutions at $Ro = -2.5$ and $\alpha = 1.8$. At these values of Ro and α, vortex breakdown results in a tripole, but for slightly more negative Ro two dipoles form instead. In figure 20(*a*), we see that the spectra for resolutions 97^3, 129^3 and 193^3 at $Re = 15$k approximately coincide with their respective maximum wavenumber. Since each simulation has different random initial conditions, we do not expect the spectra to coincide point by point, yet the overlap is very good. Each spectrum corresponds to the time $t = 175$, when centrifugal overturning is most active (i.e. when p_θ^T is near its maximum). At resolution 193^3, the spectrum shows a steep power law, perhaps as steep as k^{-6}, from about $k = 3$ to about $k = 25$, followed by a

https://doi.org/10.1017/S0022112010004945 Published online by Cambridge University Press

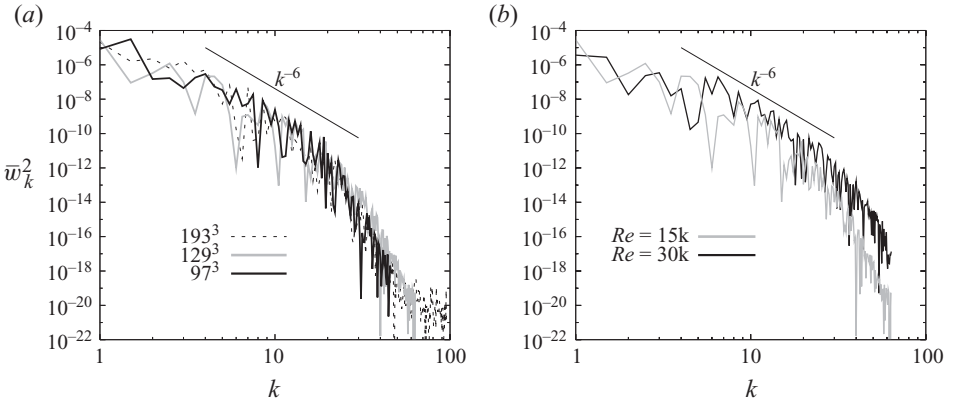


FIGURE 20. Fourier sine power spectrum of the vertical velocity w at $r = 1$ averaged over θ for simulations with $\alpha = 1.8$ and $Ro = -2.5$ taken at $t = 175$. (*a*) This plot shows how the spectrum changes for fixed $Re = 15k$ with increasing resolution: 97^3 (thick black line), 129^3 (thick grey line) and 193^3 (thin dashed line). The curve k^{-6} is shown for comparison. (*b*) This plot shows how the spectrum changes for fixed resolution 129^3 with increasing Re: grey line, $Re = 15k$; black line, $Re = 30k$.

rapid dissipation-range fall-off, into a relatively flat 'noise' range for k greater than about 55. Reaching the noise level in the spectrum is an indication of good resolution at 193^3. The k^{-6} power-law fall-off in this spectrum of the rib vortices recalls the spectrum of the Lamb dipole, which falls off similarly (Orlandi 2009). That the spectrum with resolution 129^3 matches the spectrum with resolution 193^3 up to about the noise range suggests that we have adequate resolution at $Re = 15k$ with 129^3 points. At resolution 97^3, the spectrum ends in the dissipation range, which perhaps suggests adequate resolution, but, to be safe, 129^3 resolution was used to explore the regime boundaries. For fixed resolution 129^3, as Re is increased beyond 15k, the high k spectral fall-off becomes less steep, filling in the spectrum with power-law-like behaviour out to the spectral cutoff. Figure 20(*b*) illustrates this by comparing the spectra for $Re = 15k$ and $Re = 30k$ at $Ro = -2.5$. The lack of a rapid spectral fall-off for Re beyond 15k suggested that this is the limit of the parameter range that we can explore with resolution 129^3.

REFERENCES

ARISTEGUI, J., SANGRA, P., HERNANDEZ-LEON, S., CANTON, M., HERNANDEZ-GUERRA, A. & KERLING, J. L. 1994 Island-induced eddies in the Canary Islands. *Deep Sea Res.* **41**, 1509–1525.

BARBA, L. A. & LEONARD, A. 2007 Emergence and evolution of tripole vortices from net circulation initial conditions. *Phys. Fluids* **19**, 017101.

BAYLY, B. J. 1988 Three-dimensional centrifugal-type instabilities in inviscid two-dimensional flows. *Phys. Fluids* **31**, 56–64.

BECKERS, M. & VAN HEIJST, G. J. F. 1998 The observation of a triangular vortex in a rotating fluid. *Fluid Dyn. Res.* **22**, 265–279.

BENNETTS, D. A. & HOSKINS, B. J. 1979 Conditional symmetric instability: a possible explanation for frontal rainbands. *Q. J. R. Meteorol. Soc.* **105**, 945–962.

CARNEVALE, G. F., BRISCOLINI, M., KLOOSTERZIEL, R. C. & VALLIS, G. K. 1997 Three-dimensionally perturbed vortex tubes in a rotating flow. *J. Fluid Mech.* **341**, 127–163.

CARNEVALE, G. F. & KLOOSTERZIEL, R. C. 1994 Emergence and evolution of triangular vortices. *J. Fluid Mech.* **259**, 305–331.

CARTON, X. J. 1992 The merger of homostrophic shielded vortices. *Europhys. Lett.* **18**, 697–703.

https://doi.org/10.1017/S0022112010004945 Published online by Cambridge University Press

Carton, X. J., Fierl, G. R. & Polvani, L. M. 1989 The generation of tripoles from unstable axisymmetric isolated vortex structures. *Europhys. Lett.* **9**, 339–344.

Carton, X. J. & Legras, B. 1994 The life-cycle of tripoles in two-dimensional incompressible flows. *J. Fluid Mech.* **267**, 53–82.

Carton, X. & McWilliams, J. C. 1989 Barotropic and baroclinic instabilities of axisymmetric vortices in a quasi-geostrophic model. In *Mesoscale/Synotopic Coherent Structures in Geophysical Turbulence* (ed. J. C. J. Nihoul & B. M. Jamart), pp. 225–244. Elsevier.

D'Asaro, E. A. 1988 Generation of submesoscale vortices: a new mechanism. *J. Geophys. Res.* **93**, 6685–6693.

Drazin, P. G. & Reid, W. H. 1981 *Hydrodynamic Stability*. Cambridge University Press.

Dritschel, D. G. 1986 The nonlinear evolution of rotating configurations of uniform vorticity. *J. Fluid Mech.* **172**, 157–182.

Dunkerton, T. J. 1981 On the inertial instability of the equatorial middle atmosphere. *J. Atmos. Sci.* **38**, 2354–2365.

Flament, P., Lumpkin, R., Tournadre, J. & Armi, L. 2001 Vortex pairing in an unstable anticyclonic shear flow: discrete subharmonics of one pendulum day. *J. Fluid Mech.* **440**, 401–409.

Flierl, G. R. 1988 On the instability of geostrophic vortices. *J. Fluid Mech.* **197**, 349–388.

Gallaire, F. & Chomaz, J. M. 2003 Three-dimensional instability of isolated vortices. *Phys. Fluids* **15** (8), 2113–2126.

Hayashi, H., Shiotani, M. & Gille, J. C. 1998 Vertically stacked temperature disturbances near the equatorial stratopause as seen in cryogenic limb array etalon spectrometer data. *J. Geophys. Res.* **103**, 19469–19483.

van Heijst, G. J. F. & Kloosterziel, R. C. 1989 Tripolar vortices in a rotating fluid. *Nature* **338**, 569–571.

Kloosterziel, R. C. & Carnevale, G. F. 1992 Formal stability of circular vortices. *J. Fluid Mech.* **242**, 249–278.

Kloosterziel, R. C. & Carnevale, G. F. 1999 On the evolution and saturation of instabilities of two-dimensional isolated circular vortices. *J. Fluid Mech.* **388**, 217–257.

Kloosterziel, R. C., Carnevale, G. F. & Orlandi, P. 2007*a* Inertial instability in rotating and stratified fluids: barotropic vortices. *J. Fluid Mech.* **583**, 379–412.

Kloosterziel, R. C. & van Heijst, G. J. F. 1991 An experimental study of unstable barotropic vortices in a rotating fluid. *J. Fluid Mech.* **223**, 1–24.

Kloosterziel, R. C., Orlandi, P. & Carnevale, G. F. 2007*b* Saturation of inertial instability in rotating planar shear flows. *J. Fluid Mech.* **583**, 413–422.

Knox, J. A. 1997 Possible mechanisms for clear-air turbulence in strongly anticyclonic flows. *J. Atmos. Sci.* **125**, 1251–1259.

Melander, M. V., McWilliams, J. C. & Zabusky, N. J. 1987 The axisymmetrization and vorticity-gradient intensification of an isolated two-dimensional vortex through filamentation. *J. Fluid Mech.* **178**, 137–159.

Morel, Y. G. & Carton, X. J. 1994 Multipolar vortices in two-dimensional incompressible flows. *J. Fluid Mech.* **267**, 23–51.

Orlandi, P. 2000 *Fluid Flow Phenomena: A Numerical Toolkit*. Kluwer.

Orlandi, P. 2009 Energy spectra power laws and structures. *J. Fluid Mech.* **623**, 353–374.

Orlandi, P. & Carnevale, G. F. 1999 Evolution of isolated vortices in a rotating fluid of finite depth. *J. Fluid Mech.* **381**, 239–269.

Orlandi, P. & van Heijst, G. J. F. 1992 Numerical simulation of tripolar vortices in 2D flow. *Fluid Dyn. Res.* **9**, 179–206.

Rayleigh, Lord 1880 On the stability, or instability, of certain fluid motions. *Proc. Lond. Math. Soc.* **11**, 57–70.

Rayleigh, Lord 1916 On the dynamics of revolving fluids. *Proc. R. Soc. Lond.* A **93**, 148–154.

Richards, K. J. & Edwards, N. R. 2003 Lateral mixing in the equatorial pacific: the importance of inertial instability. *Geophys. Res. Lett.* **30**, 1–4.

Sawyer, S. J. 1947 Notes on the theory of tropical cyclones. *Q. J. R. Meteorol. Soc.* **73**, 101–126.

Smyth, W. D. & McWilliams, J. C. 1998 Instability of an axisymmetric vortex in a stably stratified, rotating environment. *Theor. Comput. Fluid Dyn.* **11**, 305–322.

https://doi.org/10.1017/S0022112010004945 Published online by Cambridge University Press

Stern, M. E. 1987 Horizontal entrainment and detrainment in large-scale eddies. *J. Phys. Oceanogr.* **17**, 1688–1695.

Stone, P. H. 1966 On non-geostrophic stability. *J. Atmos. Sci.* **23**, 390–400.

Stone, P. H. 1967 An application of baroclinic stability theory to the dynamics of the Jovian atmosphere. *J. Atmos. Sci.* **24**, 642–652.

Verzicco, R. & Orlandi, P. 1996 A finite-difference scheme for three-dimensional incompressible flows in cylindrical coordinates. *J. Comput. Phys.* **123**, 402–414.

https://doi.org/10.1017/S0022112010004945 Published online by Cambridge University Press